catalysts

MDPI

Article

In-Depth Study on Synergic Interactions and Thermo-Kinetic Analysis of (Wheat Straw and Woody Sawdust) Biomass Co-Pyrolysis over Mussel Shell-Derived CaO Catalyst Using Coats–Redfern Method

Muhammad Saleem [1] and Ali Bahadar [2,*]

[1] Department of Industrial Engineering, King Abdulaziz University, Rabigh 21911, Saudi Arabia; msaleim1@kau.edu.sa
[2] Department of Chemical and Materials Engineering, King Abdulaziz University, Rabigh 21911, Saudi Arabia
* Correspondence: absali@kau.edu.sa

Abstract: The behavior of wheat straw biomass (WS), woody sawdust biomass (WB), and their blends during catalytic co-pyrolysis are analyzed in the presence of CaO catalyst, which is obtained from the calcination of mussel shells. Synergy analysis of blends and pure materials is measured by studying the difference between theoretical and experimental values of wt.%/min, (RL%), and (WL%), which correspond to maximum weight loss rate, residue left, and weight loss, respectively. The Coats–Redfern method is utilized for evaluating the thermo-kinetic properties. The chemical reaction order model F1 is the best model that describes the *Ea* of 60.05 kJ/mol and ΔH, ΔG, and ΔS values of 55.03 kJ/mol, 162.26 kJ/mol, and −0.18 kJ/mol.K, respectively, for the optimum blend 80WS−20WB, reducing the thermo-kinetic properties. Model D3 showed better results for the *Ea*, ΔH, ΔG, and ΔS for the 5% CaO blend, which certified the viability of co-pyrolysis of WS and WB, while DTG indicated that exothermic and endothermic reactions occur together.

Keywords: wheat straw; woody sawdust; co-pyrolysis; CaO; catalytic co-pyrolysis; kinetics

check for updates

Citation: Saleem, M.; Bahadar, A. In-Depth Study on Synergic Interactions and Thermo-Kinetic Analysis of (Wheat Straw and Woody Sawdust) Biomass Co-Pyrolysis over Mussel Shell-Derived CaO Catalyst Using Coats–Redfern Method. *Catalysts* **2024**, *14*, 655. https://doi.org/10.3390/catal14090655

Academic Editor: Tomás García

Received: 31 July 2024
Revised: 13 September 2024
Accepted: 16 September 2024
Published: 23 September 2024

1. Introduction

From an early period, renewable energy sources were utilized for energy-serving purposes. Wind energy for driving mills and navigation, hydropower for driving mills also, and lastly biomass sources for lighting, heating, and cooking purposes. But since the discovery of fossil fuels like coal, crude oil, and then gas, the world has shifted towards these sources in the 19th and 20th centuries. Due to the decline of fossil fuel sources and their negative influence on the environment, research on renewable energy sources has gained more importance globally [1,2]. Currently, the share of fossil fuels in the global energy mix is around 80%. The projections done by the International Energy Agency (IEA) in their World Energy Outlook 2022 reports reveal that this share will decrease to 75% by 2030 and a little over 60% by 2050. Consequently, the stake of renewable energy in the current energy mix accounts for 12% presently, reaching 17% by 2030, and by mid-century, that share will increase to 29% [3]. The utilization of renewable energy technology has grown popular in recent years. These include sources like solar, wind, geothermal, hydropower, tidal, and biomass.

Biomass is considered a primary energy source and a more stable form of renewable energy than solar and wind due to its non-effectiveness concerning weather conditions and its abundance [4]. Currently, it is the fourth-largest energy-producing source globally after oil, gas, and coal, supplying almost 14% of global energy consumption [5] and playing a key role in the whole energy system. Still, biomass has some drawbacks, like having less calorific value (CV) while producing biofuel, along with elevated oxygen and moisture content [6,7]. Solid biofuels comprise the vast majority of renewable energy output worldwide. Presently, the main source of woody biomass is agricultural waste obtained from oilseed crops and cereal, the food and wood processing industry, and forests [8]. Wood biomass, both from agricultural short-rotation-woody-crops (SRWC) cultivation and forest-derived, is utilized as raw material for heat and electricity production through gasification [9]. One of the wastes produced from processing forest-derived wood biomass used for doors in construction is called sawdust, which is presently studied extensively for its potential utilization in biofuel production [10]. Woody sawdust (WB) is considered an excellent renewable energy source, containing a lower ash content and higher heating value, along with conversion towards excellent quality pyrolysis products [11]. Another biomass source that is obtained from the waste of one of the world's most important crops related to agriculture is wheat straw (WS), which contains higher ash content than woody sawdust (WB). Wheat is a main food crop, so it has ginormous production. The structure of WS mainly constitutes lignin, hemicellulose, and cellulose; the latter ones entail complicated amorphous structures. While analyzing its dry weight, WS consists of 17.1% lignin, 39.5% hemicellulose, and 38.8% cellulose [12]. There are significant differences between forestry residue and agricultural residue, including the percentage of the main components and the contents of other elements, which will help in understanding the interactions between the different biomass materials in thermochemical processes, which are extremely complex.

Thermogravimetric analysis (TGA) is an important tool for measuring biomass mass loss and pyrolysis kinetic characteristics throughout the thermal degradation process [13]. Pyrolysis kinetics, mechanism, and thermodynamics must be studied to design co-pyrolysis reactors, maximize desired product output, and optimize process variables. Today, most nations focus on replacing conventional transportation fuels with ecologically friendly alternatives, such as biofuels [14,15]. The study of chemical kinetics and thermodynamics characteristics using TGA is essential because it reflects whether or not the examined materials are suitable for use as an alternate source [15]. Co-pyrolysis is a process in which two or more feedstocks as raw materials are utilized. In any co-thermochemical process, it is the essential first step, and the benefits of this process include uniqueness related to biofuel production like syngas, bio-oil, and biochar [16]. Biomass co-pyrolysis has gained popularity as a viable technique for producing bio-oil, which may then be utilized as a sustainable energy source [17]. Even while co-pyrolysis of two biomass raw materials may result in a higher grade bio-oil, it still has a high oxygen content and a poor heating value [18]. However, these disadvantages can be mitigated, to some extent, through a catalytic approach [19] to improve the product yields and selectivity along with catalyst efficiency, meanwhile reducing coke formation and pyrolysis temperature; an advanced pyrolysis technique, namely catalytic co-pyrolysis, is utilized [20,21]. This type of catalytic co-pyrolysis can be of two types based on the mixing of the sample. If the blends are pyrolyzed separately and then passed downstream where the catalyst bed is located, then it is called ex situ. And, if the samples are directly mixed with the blends, it is called in situ [22].

Calcined dolomite [23], HZSM-5 [24], Cu/C, Pd/C, and Pd-Ag [25] were studied as catalysts for utilization in the catalytic pyrolysis of sawdust by the researchers. Fe-Ca-Ni [26] and HZSM-5 [27] were studied as catalysts for utilization in the catalytic pyrolysis of WS. Various studies have been performed on catalytic co-pyrolysis of WS with plastics to study their kinetics via model-fitting and model-free techniques [18,28,29]. However, very little study has been conducted on the co-pyrolysis and the catalytic co-pyrolysis of one biomass along with another biomass feedstock. The majority of biomass pyrolysis and biomass catalytic pyrolysis research has been conducted utilizing a single feedstock, with a particular focus on their usage as a source of valuable chemicals [30]. CaO is a heterogenous catalyst with advantages like cost-effectiveness, environmentally friendly, easy to handle, and elevated basicity [31]. CaO was also utilized in the microwave-assisted catalytic pyrolysis of biomass for bio-oil production [32]. Xue et al. performed a study in which CaO was coupled with ZSM-5 zeolite as a dual-layer catalyst for the catalytic pyrolysis of poplar sawdust [33]. Dzol et al. conducted a study in which they compared the performance of various catalysts, among which CaO was included, against waste cooking eggshell (WCE) in catalytic pyrolysis [34]. Chen et al. performed a study in which CaO-based catalysts were analyzed in the catalytic co-pyrolysis of corn husk (CH) and food waste digestate (FD) for upgrading bio-oil [35]. The results revealed that the yield of bio-oil production increased with CaO catalysts. CaO was also utilized as a catalyst in the catalytic co-pyrolysis of biomass and plastic to increase bio-oil yield [36]. The focus of this research is to evaluate the effect of in situ catalytic co-pyrolysis via TGA and to study the interactive behavior among the two biomasses to improve the quality of the product bio-oil by deoxygenation using CaO catalytic upgrading. To the best of the authors' knowledge, no comprehensive study has been reported so far on the application of mussel shell-derived CaO catalyst on (wheat straw and woody sawdust) biomass co-pyrolysis for a better yield of bio-oil produced.

In the present study, woody sawdust and wheat straw were blended in various ratios for the first time and then characterized using different techniques such as FTIR (Fourier transform infrared spectroscopy), GCV, and CHNS-O (ultimate analysis). CaO catalyst was characterized via FTIR, XRD, and SEM-EDS. A thermogravimetric analyzer (TGA) was utilized for performing the co-pyrolysis in an inert environment and evaluating thermo-kinetic behavior. For the identification of an optimum blend, synergy analysis was utilized. The mechanistic behavior was evaluated by utilizing the Coats–Redfern fourteen (14) integral technique, and thermodynamic parameters like ΔS, ΔG, and ΔH were also studied. Furthermore, the CaO catalyst was utilized for studying the optimum blend's catalytic co-pyrolysis and is compared with the optimum blend to have insights for future use.

2. Results and Discussion

2.1. Physiochemical Characterization

The ultimate analysis (CHNS-O) and Gross Calorific Value (GCV) of pure wheat straw (100WS) and woody sawdust biomass (100WB) are shown in Table 1. Both biomass samples have varied compositions since each of them has distinct formation characteristics and origins that might cause an increase or decrease in specific components and phases [37]. The carbon content of 100WS was roughly 41.25%, nearer but lesser than 100WB, which was 47.20%. In the research studies, alike carbon composition for 100WS and 100WB has been reported [5,38]; thus, 100WB will have a higher char yield attained if the fuel contains a higher quantity of carbon [39]. The amount of hydrogen in 100WS and 100WB samples was 5.85% and 7.20%, respectively, displaying that they are also nearly adjacent to one another and that woody sawdust biomass waste has a higher hydrogen content than wheat straw waste. Although the nitrogen content of 100WS was 0.62%, for 100WB, it was 0.12%, which is almost five times lower than that of 100WS; in some studies, almost a comparable amount of nitrogen in wheat straw was stated [38], while also nearly similar results in literature were reported for 100WB [5]. The sulfur content of 100WS was 0.16%, which was higher than that of 100WB, for which it is 0.02%, which is nearly equal to zero; similar results were found in the literature for 100WS and 100WB [40]. The oxygen content was higher in 100WS as compared to 100WB. The energy content H/C and O/C ratios for 100WS were 1.69% and 0.95%, while for 100WB, they were 1.82% and 0.72%. Because biomass has a higher H/C ratio than other materials, it supplies more hydrogen resources to play a leading role in hydrogenation [41]. The H/C value is responsible for energy content; consequently, it will improve the combustion process [42]. The presence of H, N, and S collectively was slightly high in 100WB in comparison to 100WS since it has these elements as their main constituents, whilst carbon presence in 100WB was higher. After all, it is its main component. The energy content in a fuel is briefly defined by GCV, which is its important property [43]. The GCV of 100WS and 100WB specifically demonstrates the heat of combustion, which was determined by a Parr 6200 oxygen bomb calorimeter. The GCV of 100WB was higher than that of 100WS, which surely shows that woody sawdust biomass waste has higher carbon content and less moisture content than 100WS, as shown in the ultimate analysis presented in Table 1.

Table 1. Ultimate analysis of wheat straw and woody sawdust biomass.

Sample Code	Carbon (%)	Hydrogen (%)	Nitrogen (%)	Sulfur (%)	Oxygen [a] (%)	O/C (%)	H/C (%)	GCV (MJ/kg)
100WS	41.25	5.85	0.62	0.16	52.12	0.95	1.69	17.92
100WB	47.20	7.20	0.12	0.02	45.46	0.72	1.82	20.80

[a]—by difference.

The FTIR spectrum of (WS−WB) blends is depicted in Figure 1. There may be substantial distinctions between them in the key functional groups on the biomass surface due to the difference in their compositions. This technique aids in the research of material structure and properties, revealing vital data about their chemical structure.

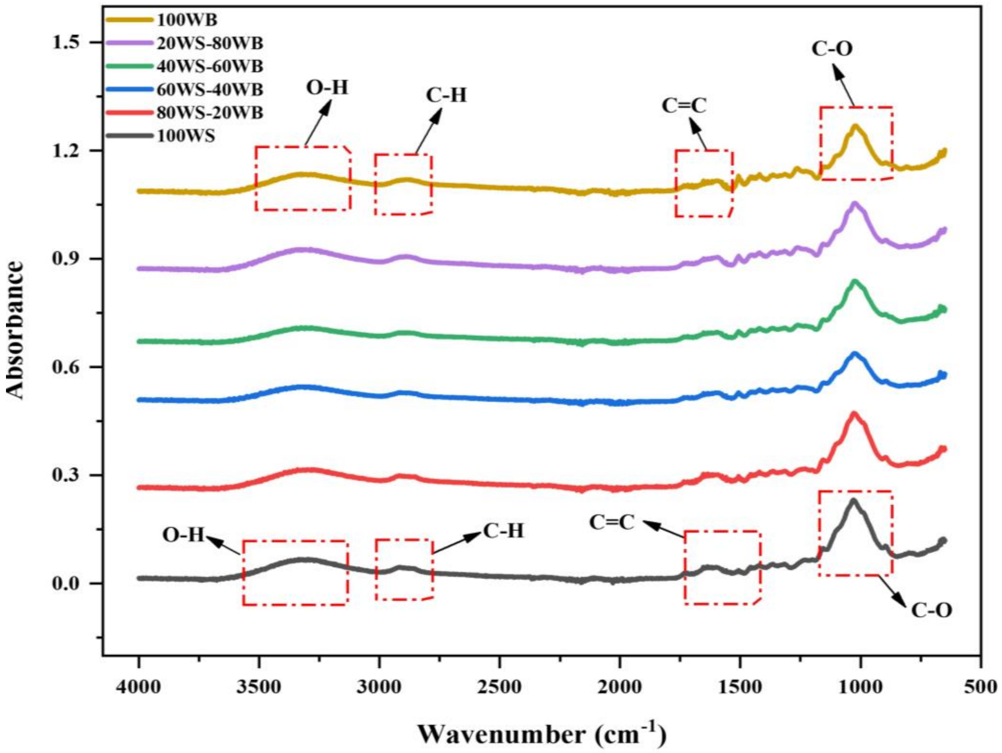

Figure 1. FTIR of WS−WB blend.

The FTIR spectra of 100WS disclose a broad absorptional vibration peak at 3325 cm^{-1}, indicating hydroxyl (O-H) stretching. This group's existence indicates the existence of alcoholic, hydroxyl, and phenolic group attachments and is found abundantly in all types of biomasses, which shows that it contains hydrogen and oxygen in large amounts [44]. A small widening peak exists at 2905 cm^{-1}, which shows the existence of -CH aliphatic stretching in polysaccharides. Due to the existence of a high carbon amount found in the ultimate analysis, a vibration peak stretching is indicated at 1620 cm^{-1}, showing the presence of C=C aromatic stretching vibration. C-O stretching is observed at 1025 cm^{-1}, depicting the presence of cellulose, hemicellulose, and lignin [45], as depicted in Figure 1. In 100WB, obvious broadening and stretching peaks were detected at 3320 cm^{-1}, which depicts the hydroxyl (O-H) stretching, the same as for 100WS; this peak exists as a major peak in all biomasses and relates to moisture presence. A small peak at 2890 cm^{-1} depicts cellulose existence, marks the existence of a methylene group in the cellulose and is assigned as an aliphatic C-H stretching vibration. Furthermore, a weak and strong peak was observed at 1596 cm^{-1} and 1025 cm^{-1}, which depicts the existence of aromatic C=C stretching vibration and lignin existence and is also accredited to the benzene ring in its molecules, highlighting nitrogen presence in the ring [46]. The strong peak depicts the existence of C-O stretching vibration, which indicates the 100WB network ordinarily contains alcoholic and phenolic

O-H groups and sometimes an ether bond. In literature, approximately the identical peak for C-O stretching vibration for cellulose and hemicellulose is reported [47].

The majority of the peaks found in 100WS, 100WB, and WS−WB blends had identical wavenumbers with variations in absorbance. Furthermore, it can be shown that the functional groups in the 100WS and 100WB samples of biomass are similar, but their intensity of absorption or percentage of their relative contents are different. The peaks existing in blends (80WS−20WB), (60WS−40WB), (40WS−60WB), and (20WS−80WB) are shown in Figure 1. The peak mentioned at (3320–3325 cm^{-1}), (2890–2900 cm^{-1}), (1596–1620 cm^{-1}), and at the 1025 cm^{-1} region slightly varies between 100WS and 100WB, showing their dominance. Thus, when 100WS is mixed with 100WB, the functional group intensity changes, so WS-WB mixtures show the intermediary actions concerning band intensity in between the parent bandwidth of both 100WS and 100WB.

2.2. Catalyst Characterization

Figure 2 represents the FTIR configuration of the prepared catalyst over the range of 650–4000 cm^{-1}. There are multiple peaks in the spectrum that represent the existence of various groups. The spectrum peak at 866 cm^{-1} was determined as the out-of-plane vibration modes of the carbonated group (CO_3^{-2}) [48]. The spectrum peak at 1132 cm^{-1} with low intensity was attributed to stretching vibrations of C−O bonds [49]. Furthermore, a strong peak was observed at 1411 cm^{-1}, which was a clear representation of the C=O group's asymmetric stretching in CO_3^{-2} ions [50,51]. The strongest peak was detected at 3636 cm^{-1}, which was attributed to the stretching peak of the hydroxyl group. This corresponded to the absorption of water on the surface of the prepared catalyst [31,51]. The details of the FTIR spectrum data of the CaO catalyst are given in Table 2. As seen in Figure 2, there are four peaks observed on the spectrum. Each peak range represents a respective functional group that is present in the catalyst. FTIR is capable of detecting functional groups, such as CO_3^{-2}, even in trace amounts that may not result in detectable crystalline phases in XRD. This notable sensitivity to small quantities clarifies why carbonate peaks manifest in the FTIR spectrum even when they are not discernible in XRD [52,53].

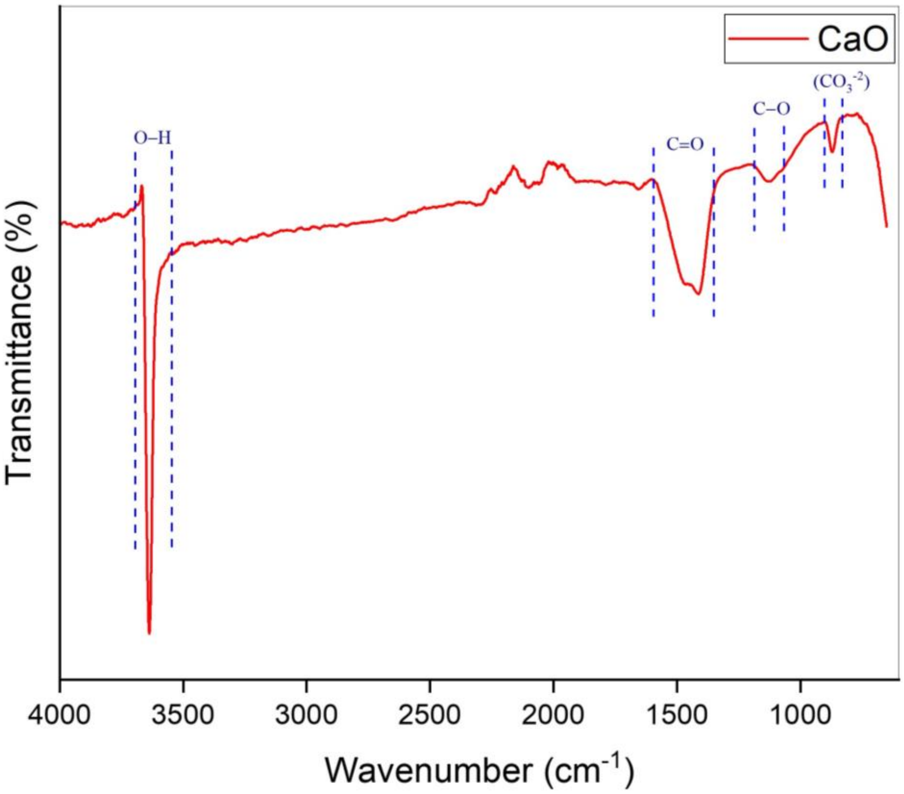

Figure 2. FTIR Spectrum of CaO.

Table 2. Details of CaO catalyst FTIR spectrum.

CaO Catalyst				
Sr No.	**Range**	**Peak**	**Functional Group**	**Reference**
1	833–896	866	$CO_3{}^{-2}$	[48]
2	1064–1186	1132	C−O	[49]
3	1337–1580	1411	C=O	[50,51]
4	3551–3691	3636	O−H	[31]

XRD was utilized to investigate the structure of CaO. Table 3 demonstrates the lattice parameter, interplanar spacing, phases, and crystallite size, which have been effectively charted out by the analysis of the crystal structure. The diffraction follows Bragg's equation (Equation (1)), where n = integer, λ = wavelength of light, d = spacing between crystal planes in the material, and θ = angle of incident light. For calculating interplanar spacing "d", Bragg's formula was utilized as shown in Equation (1) [54]:

$$N\lambda = 2d\sin\theta \tag{1}$$

where the inter-planar distance between two neighboring planes in the (hkl) family is represented by "n". The following expression in Equation (2) is obtained by utilizing Bragg's formula in Equation (1) [55]. This expression gives us the lattice parameters.

$$\frac{1}{d^2} = \frac{\left(h^2 + k^2 + l^2\right)}{\alpha^2} \tag{2}$$

Table 3. Details of CaO's XRD measurement.

Angle "2θ" (°)	Interplanar Spacing "d" (Å)	FWHM (Radians)	Crystallite Size "D_s" (nm)	Lattice Parameters "a = b = c" (Å)
32.20	2.78	0.059	146.4	1.079852
37.35	2.40	0.072	121.7	1.662741
53.85	1.70	0.096	97.02	4.700846

A mathematical representation of Scherer's formula for calculating the crystallite size of the XRD peaks by utilizing FWHM (full width at half maximum) is represented by Equation (3) [54].

$$D_s = \frac{0.9\lambda}{\beta\cos\theta} \tag{3}$$

Here, the Bragg diffraction angle is represented by θ, FWHM is denoted by β given in radians, the constant wavelength of the X-ray is given by λ, k represents the shape factor given as 0.9, and the crystallite size is given as D_s.

Substantial peaks are identified between 30° and 60°, as shown in Figure 3. The catalyst revealed peaks at multiple angles. The first peak was recorded at 32.20°, and its intensity is lowest when compared with the intensity of other peaks. This peak corresponded to the (111) plane of the CaO. After that, a strong peak was observed at 37.35°, which corresponded to the (200) plane of the CaO. The third peak was observed at 53.85°, which corresponded to the (220) plane of CaO. These findings correlated with JCPDS card No. 37-1497 of the Joint Committee on Powder Diffraction Standards. The cubic phase of the catalyst was determined by the XRD pattern. Sharp XRD reflections ((111), (200), and (220)) indicate that the catalyst is well crystallized [56]. Furthermore, no secondary phases were detected, such as $CaCO_3$. The average crystallite size of the catalyst CaO was calculated to be 121.70 nm. A space group of Fm-3 m (225) was detected for CaO. X-ray diffraction (XRD) is most useful for identifying crystalline phases. If the carbonate is present in an amorphous form or in very small quantities, it may not generate detectable peaks in XRD.

This limitation clarifies why XRD might not identify $CaCO_3$, even if $CO_3{}^{-2}$ is present in the sample [57].

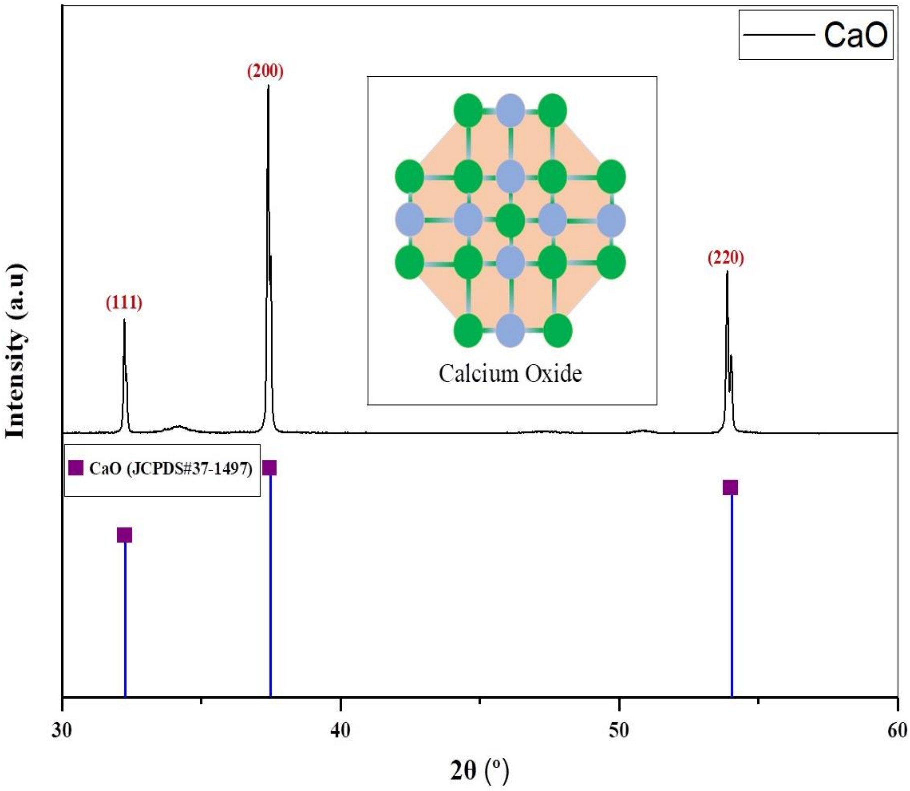

Figure 3. Diffractogram of CaO catalyst.

Scanning Electron Microscopy (SEM) was utilized to examine the morphology and structure of the CaO catalyst. Figure 4a represents the SEM image of the CaO catalyst at 2 µm. The structure resembles a needle-like shape with varying height and thickness. In other words, it can also be termed a worm-like structure. Furthermore, the porosity in the structure is visible, which can be ascribed to the release of CO_2 and water during calcination. In this way, water and CO_2 could be attributed as porogens. An increase in catalytic activity is observed due to this porous surface [56]. A crystalline structure is observed, which is also attributed to the calcination of $CaCO_3$ [31]. The EDS analysis revealed that the elemental composition of CaO includes 53.74% w/w Ca and 43.85% w/w oxygen, as depicted in Figure 4b. The presence of carbon in SEM-EDS is most likely attributed to surface contamination or the adsorption of atmospheric CO_2, a prevalent issue in SEM-EDS analysis, where surface elements may not accurately represent the bulk material [58]. There are various organic impurities present in minute quantities that can be detected by SEM-EDS and FTIR but not enough to be detected by XRD [59].

Figure 5 represents the color-mapped SEM image of the CaO catalyst. The calcium content is represented by red color, and the green dots represent oxygen. As depicted in the EDS analysis in Figure 5, Ca is spread all over the sample, and oxygen is present in clusters, which explains the higher w/w% of Ca in the specimen. The oxygen clusters depict a dense structure when compared to Ca, which is evenly spread across the specimen. The bonding between the particles and their irregular shape is attributed to the calcination of $CaCO_3$.

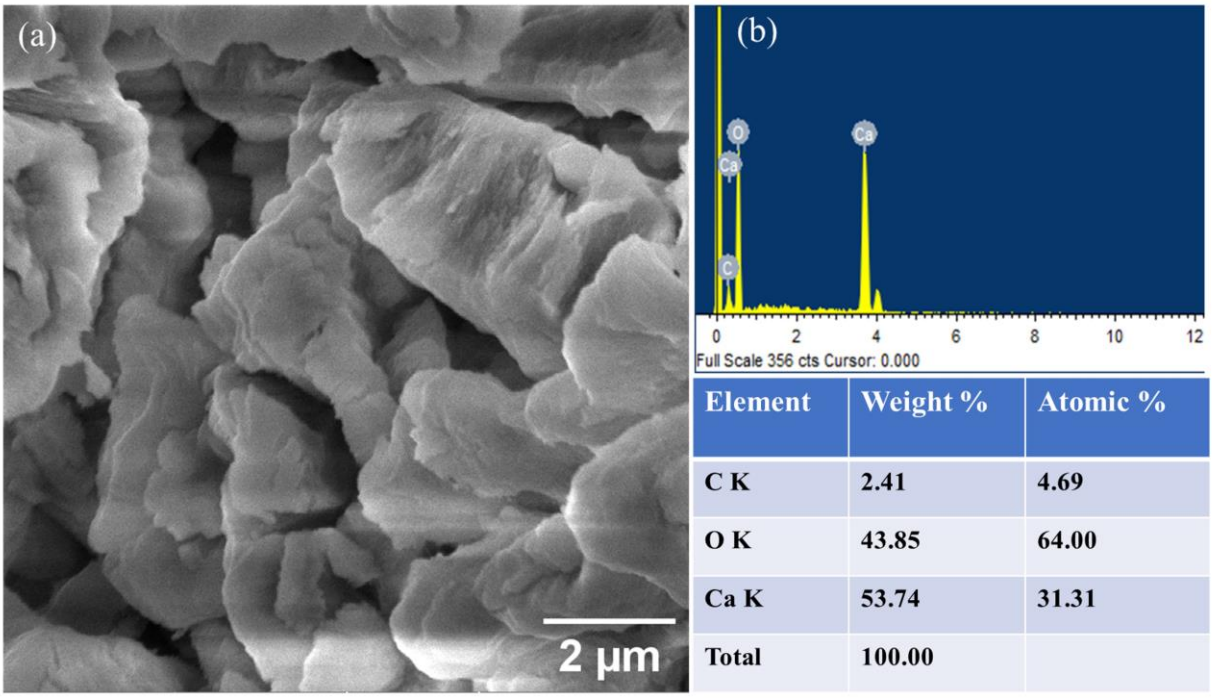

Element	Weight %	Atomic %
C K	2.41	4.69
O K	43.85	64.00
Ca K	53.74	31.31
Total	100.00	

Figure 4. SEM image of CaO catalyst (**a**) at 2 µm and (**b**) EDS with element weight %.

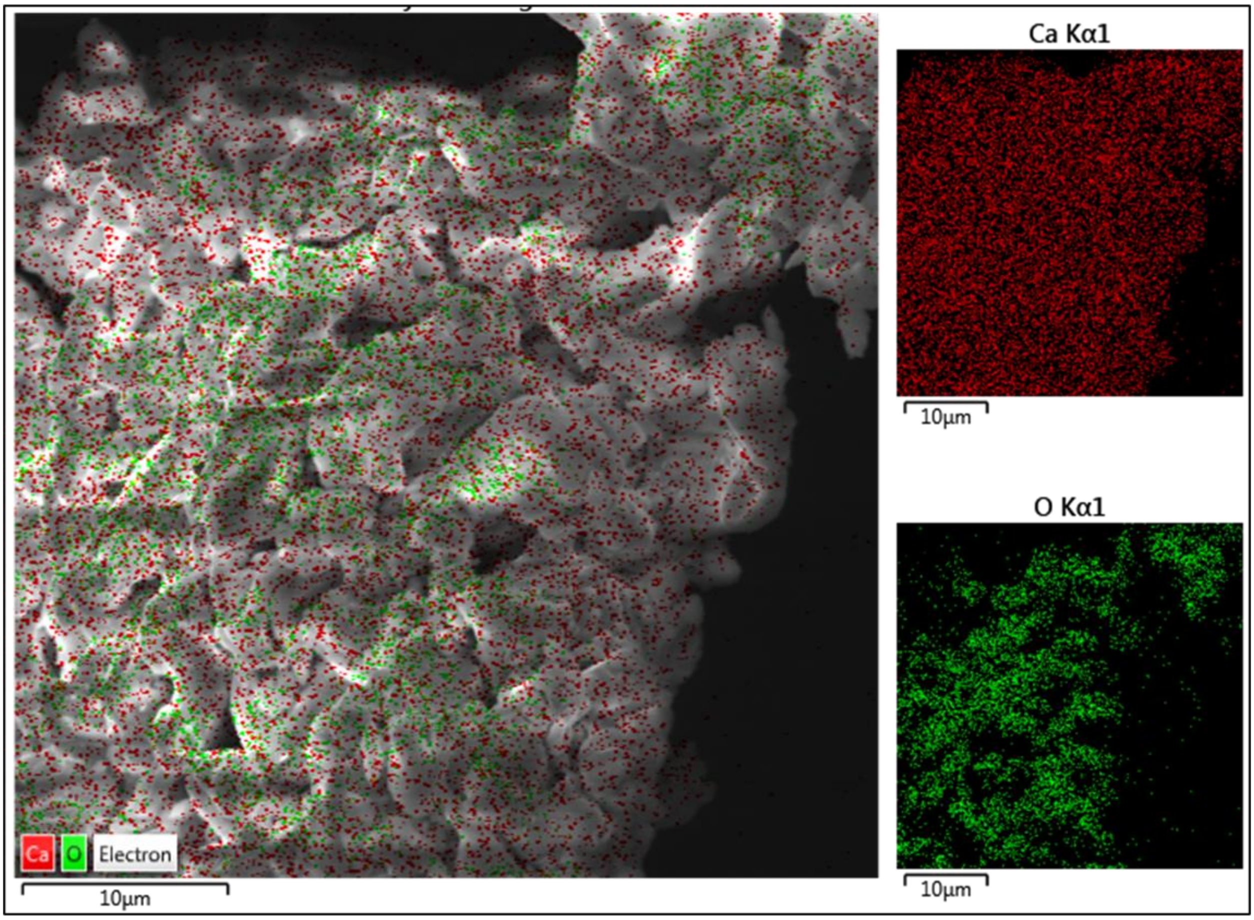

Figure 5. Color mapping SEM image of CaO catalyst.

Figure 6 depicts the analysis of particle size measurement for the CaO catalyst. Since the catalyst showed a worm-like structure, the thickness of various particles, which can be seen in Figure 6a, is measured using ImageJ software version 1.54g (National Institute of Health, Bethesda, MD, USA). Since the particles are stacked over each other in an irregular manner, only the visible particles are taken into account for the thickness/diameter measurement. After calculating the diameter of various samples, we plot the data in the form of a histogram for better understanding. The mean diameter of the CaO catalyst was calculated to be 1.66 μm, as represented in Figure 6b.

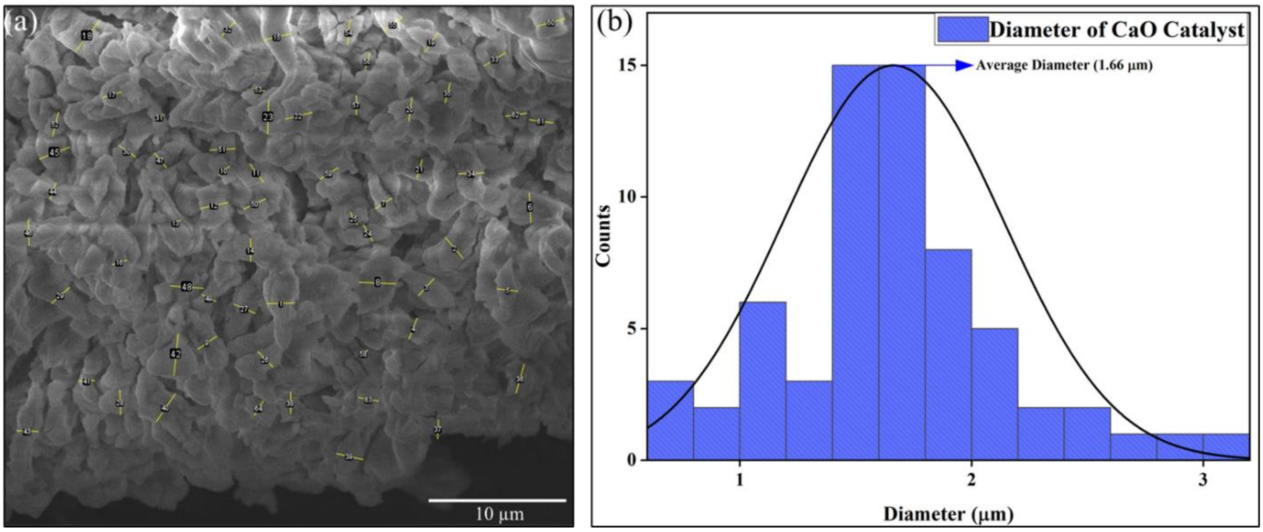

Figure 6. Particle size analysis of CaO catalyst: (**a**) SEM image and (**b**) graph.

2.3. TGA

The weight loss behavior of (WS−WB) blends concerning temperature and its first derivative (DTG) in (wt.%/min)'s terms were examined by the thermogravimetric analyzer (TGA), which can be seen in Figure 7a,b. The weight loss of (WS−WB) blends was categorized by a three-stage thermal process, irrespective of their nature [60]. Those three stages include the first stage, known as the moisture removal stage, which lies in the temperature range of (25–150 °C); the second stage, known as the devolatilization stage, occurs in the temperature range of (200–500 °C); and the third stage, known as slow degradation of the solid residue, which lies in the temperature range of (500–900 °C).

For 100WS, slight weight loss occurs due to the removal of bound and inbound watery components and volatiles in the form of non-condensable and condensable gases from the material in the first stage [61]. In the second stage, rapid and most of the material's weight loss was witnessed from the sudden slope that develops in DTG curves; degradation of cellulose and hemicellulose was responsible for occurring in the temperature range of (200–450 °C). Whereas in the third stage, the reactions occur at a high temperature where slow degradation occurs, mostly attributed to the carbon residues and lignin due to their complicated structure, and they degrade at a very slow rate due to the difficulty in breaking them down [62]; this is responsible for methane and hydrogen gas generation [63], as shown in Figure 7a. The TGA curve presents 100WB degradation in three stages. In the first stage, moisture removal and marginal loss of light volatiles occur. Structural water that exists in the form of H and OH moieties is exposed from the equatorial point of cellulose in the temperature range of (140–150 °C) [64]. The second stage for 100WB lies in the temperature range of (200–480 °C), where a sharp decrease was noted during its degradation of cellulose and hemicellulose, nominated as an active pyrolysis zone. The third stage occurs in the temperature range of (500–900 °C) and is ascribed to the degradation of lignin and carbonaceous material, which eventually degrades at a very slow rate, as depicted in Figure 7a. The co-pyrolysis of the four (WS−WB) blends, i.e., (80WS−20WB), (60WS−40WB), (40WS−60WB), and (20WS−80WB), is also displayed in three stages. The difference between the profiles of thermal degradation of samples is well understood. In the first stage, the removal of moisture occurs the same as the parent materials. The second stage lies in the temperature range of (200–500 °C) and is known as the active pyrolysis region, where the main constituent of both biomasses, i.e., hemicellulose, degrades first, and then cellulose degrades in this region. The third stage occurs in the temperature range of (500–900 °C), where the free radicals formed in both biomasses help each other in the degradation of lignin in this stage. The breaking of various bonds occurs due to the volatile formation from the blends, as shown in Figure 7a. The weight loss behavior of the constituent materials is imitated by the blends during co-pyrolysis, subjective to blending ratios. When the amount of 100WB in the blends was increased, the (WL%) also increased, which suggests that there is more volatile content in 100WB than in 100WS [65].

The maximum weight loss rate that takes place at which temperature in the course of the process is the maximum reactivity temperature peak in the DTG curve and is described in terms of (wt.%/min); two peaks were observed in the first two stages of (WS−WB) blends. The maximum degradation rate in the first stage for 100WS and 100WB was found to be −0.7753 and −0.6572 wt.%/min at 53.89 °C and 51.83 °C. For the four (WS−WB) blends, i.e., (80WS−20WB), (60WS−40WB), (40WS−60WB), and (20WS−80WB), the maximum degradation rate was (−0.9044 wt.%/min), (−0.8175 wt.%/min), (−0.5582 wt.%/min), and (−0.7033 wt.%/min) at 56.65 °C, 55.03 °C, 66.24 °C, and 59.03 °C, respectively, as presented in Figure 7b. At the beginning of the second stage of thermal degradation of 100WS, a minor shoulder curve was observed between (250–320 °C), whereas in 100WB, a major shoulder curve was detected between (300–350 °C) in DTG, while in the four (WS−WB) blends, two peaks exist. The first peak was prominent, large, and sharp and was like a shoulder curve, while the second one was small, known as the primary peak, where a rapid weight loss was examined as the slope increased in the DTG curves; thus, the degradation reached a peak then decreased as the temperature further increased. Hemicellulose and cellulose degradation occurs in this stage and is accountable for massive weight loss. The shoulder curve simply represents the degradation of hemicellulose that occurs between (250 and 350 °C), which was followed by a primary peak, which is attributed to the degradation of cellulose, mostly happening in the later part of the second stage in the parent materials and their blends. At the end of this stage, complete depletion of volatile matter content in 100WS occurs. The maximum degradation rate in the second stage for 100WS and 100WB was found to be −9.2283 wt.%/min and −8.3836 wt.%/min at 329.02 °C and 368.06 °C; similar peak temperatures were reported in the literature for 100WS and 100WB [46,64]. For the four (WS−WB) blends, i.e., (80WS−20WB), (60WS−40WB), (40WS−0WB), and (20WS−80WB), the maximum degradation rate was (−8.2449 wt.%/min), (−7.1169 wt.%/min), (−6.044 wt.%/min), and (−5.9499 wt.%/min) at 330.1 °C, 329.79 °C, 344.19 °C, and 332.34 °C, respectively, as presented in Figure 7b. The third stage has no sharp peaks detected in the DTG curve for the (WS−WB) blends, as it follows a smooth horizontal line from 500 °C until 900 °C, as shown in Figure 7b. The peak intensity of the blends varies among the peaks of 100WS and 100WB. The peak degradation temperature of (WS−WB) also varies between the parent materials. Also, the T_p of 100WB was lowered from 368 °C through blending with 100WS, showing its reactivity dominance, as 100WB has a higher T_p than 100WS. At the reaction's end, the complete (WL%) was 72.35%, 74.62%, 74.95%, 73.96%, 79.18%, and 82.98%, while the (RL%) was 27.65%, 25.38%, 25.05%, 26.04%, 20.82%, and 17.02% at 0, 20, 40, 60, 80, and 100% of woody sawdust biomass, respectively.

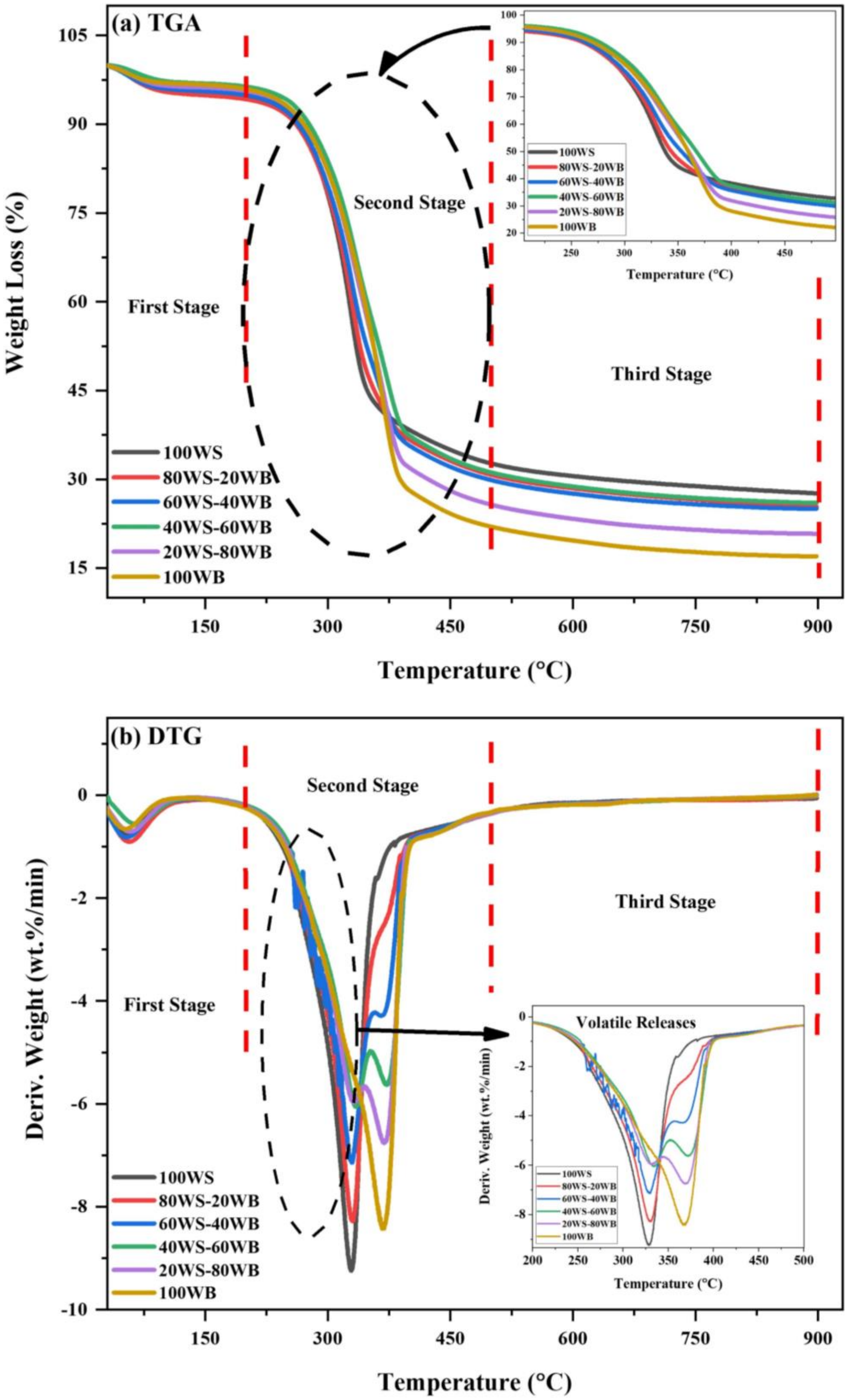

Figure 7. (**a**) TGA and (**b**) DTG curves of (WS−WB) blends in N_2 atmosphere.

Synergy Analysis

100WS and 100WB showed different thermal behaviors due to the alterations in their chemical and structural properties in the main constituents. To get an in-depth understanding of the thermal behavior of the blend synergy, an analysis study of (WS−WB) blends was carried out. An additive formula was utilized, presuming that there was no interaction between the two substances in the blend (WS and WB). The thermal profile was calculated employing the additive formula by comparing it to the experimental results. The synergy analysis might be extrapolated from the difference between the two profiles. The blends' calculated and experimental TGA curves are plotted in Figure 8. Table 4 examines the highest relative deviations among the blends' calculated and experimental TGA curves. The production of more volatiles in co-pyrolysis than individual pyrolysis is a result of a positive synergy analysis value [66]. Synergy analysis is also aided by heat transfer during co-pyrolysis. The generation of radicals through reactions that include intermolecular hydrogen movement, depolymerization, and isomerization is well recognized for influencing co-pyrolysis [67]. The synergy analysis of free-radical processes in the co-pyrolysis process results in better biofuels that have a high GCV [64].

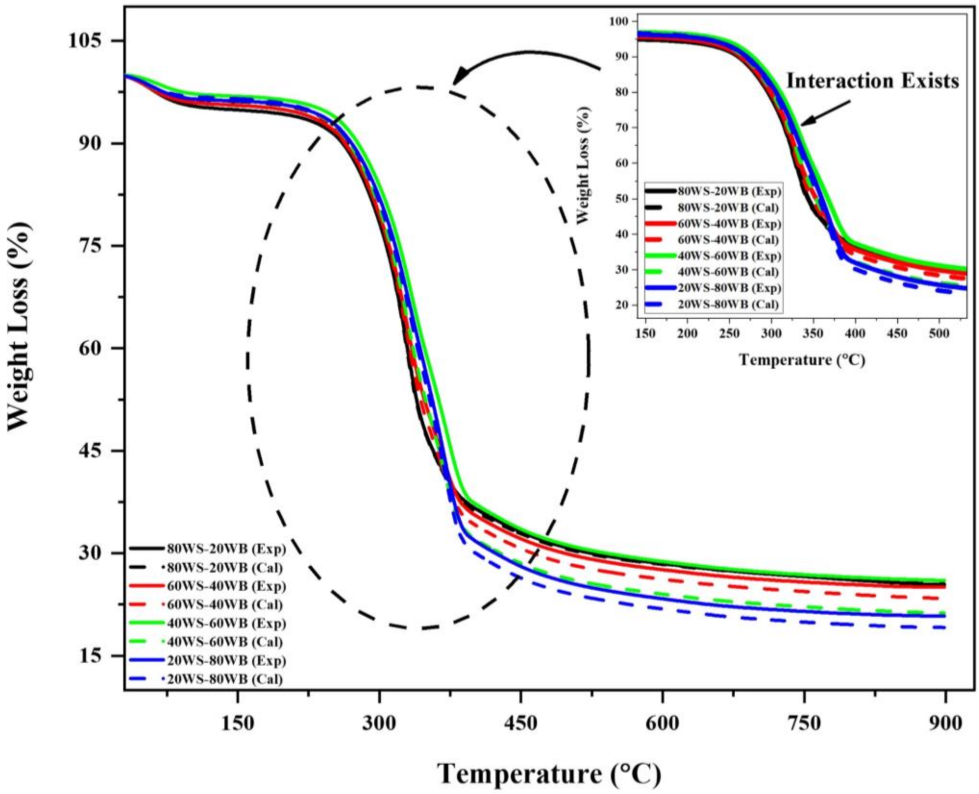

Figure 8. Synergy analysis evaluation of (WS—WB) blends in N_2 atmosphere.

Table 4. Synergy analysis evaluation of (WS-WB) blends.

Sample Code	Experimental Value (S_E)		Calculated Value (S_C)		Deviation (%)	
	(WL%)	(RL%)	(WL%)	(RL%)	(WL%)	(RL%)
100WS	72.35	27.65	-	-	-	-
80WS—20WB	74.62	25.38	74.48	25.52	0.19	−0.54
60WS—40WB	74.95	25.05	76.60	23.40	−2.15	7.05
40WS—60WB	73.96	26.04	78.73	21.27	−6.06	22.43
20WS—80WB	79.18	20.82	80.85	19.15	−2.07	8.72
100WB	82.98	17.02	-	-	-	-

From the TG curve, we can see that for 80WS—20WB and 60WS—40WB, the calculated curve value was higher than the experimental curve until it reached 300 °C, where it remained negative; after that, the experimental curve value got higher and showed significant positive synergy analysis in the second stage of TG and remained positive until it reached 900 °C. Whereas in 20WS—80WB in the first stage, it was positive at first and then got negative synergy analysis; after that, in the second stage, after 250 °C, it remained positive until it reached the end at 900 °C. For 40WS−60WB, it remained positive in all three stages of degradation in TG. The deviation values of the synergy analysis are shown in Table 4. The positive synergy analysis regarding (WL%) is simply due to the release of volatiles; they were all preferred for bio-oil and biogas production, and the deviancy in the values is higher in terms of (WL%) for 80WS−20WB. While the negative synergy analysis in regard to (RL%) shows that they were all preferred for biochar [66], in terms of (RL%), 60WS−40WB, 40WS−60WB, and 20WS−80WB are the best. Positive synergy analysis with regard to (RL%), together with a negative result in (WL%), suggest that the provided sample is ideal for the yield of biochar and vice versa. So, based on synergy analysis, 80WS−20WB is evaluated as an optimum blend. Figure 9 represents the possible synergy mechanism during the co-pyrolysis of WS and WB.

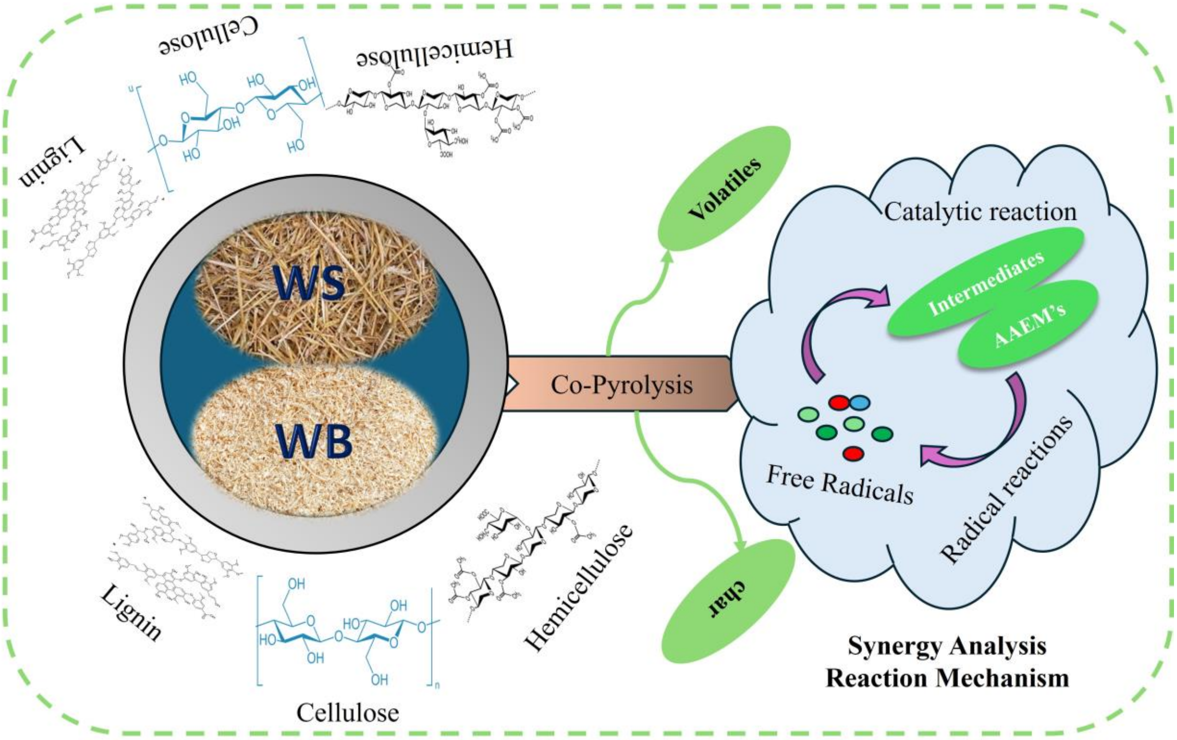

Figure 9. Possible synergy mechanism during co-pyrolysis of WS and WB.

2.4. Thermo-Kinetic Modeling

The data taken from (WS−WB) blends' co-pyrolysis through TGA at a heating rate of 10 °C/min, which is represented in Figure 10a–d and Table S1, resulted in the calculation of kinetic triplets. The goal of fourteen G(α) is to find the most effective reaction mechanism for each level of WS−WB blends. The analysis in fourteen G(α) was based on larger R^2 values, with the specified range from 0.90 to 0.99 [68,69]. The activation energy was calculated by using the slope of the plot. The kinetic investigation was conducted on the active pyrolysis zone since it has a higher percentage of (WL%) [70]. The smallest amount of energy necessary for starting a reaction is called Ea, while for starting the reaction, the number of clashing molecules in the required direction is denoted by A [71]. The sample reactivity is determined by Ea, while A is primarily concerned with the material structure [60]. The main pyrolysis region for the volatile releases can be considered as the single main process region with a single Ea, R^2, and A. The rapid degradation region lies in the overall temperature region of (180–430 °C).

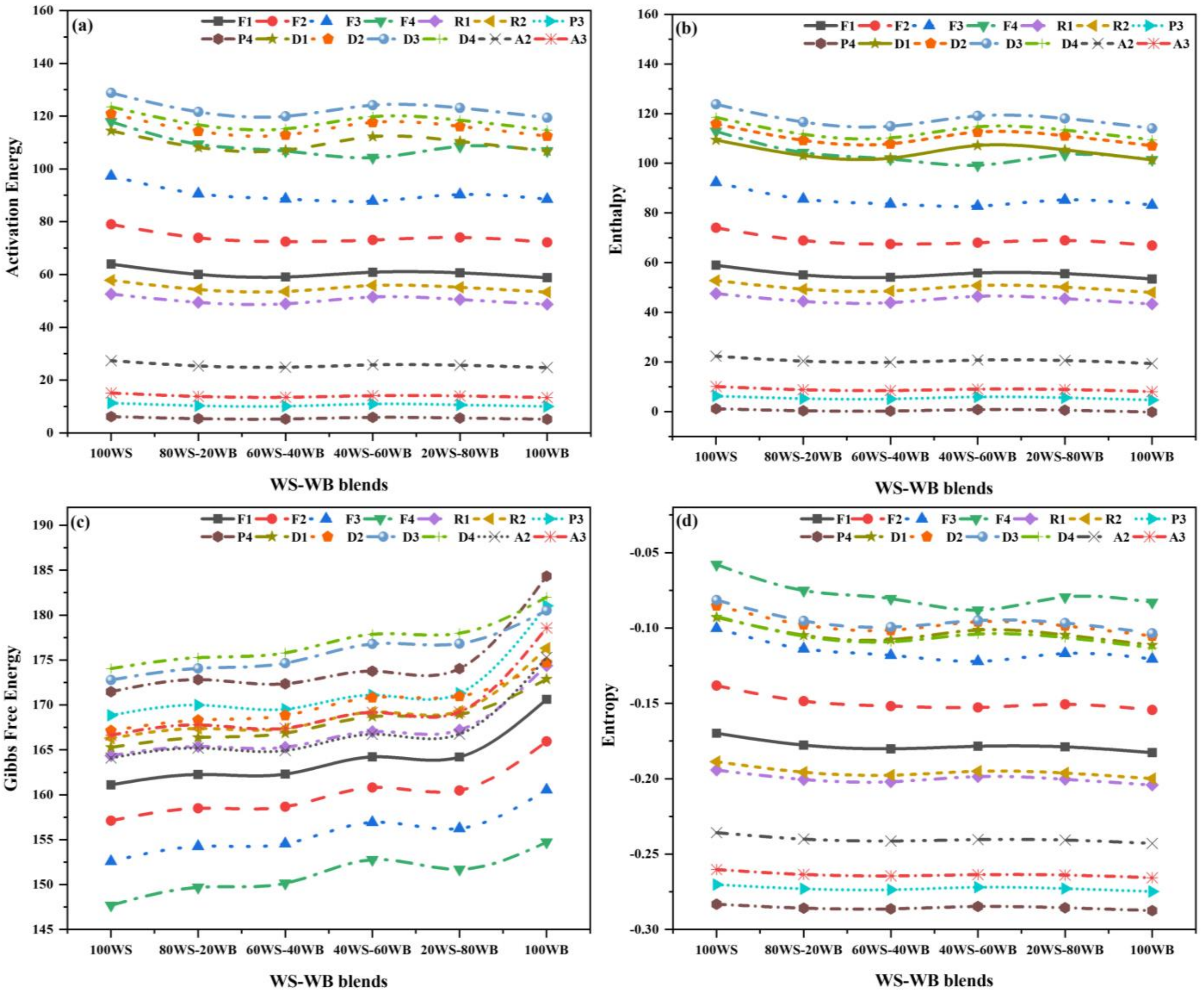

Figure 10. Thermo-kinetic properties for different models of WS−WB blends: (**a**) *Ea*, (**b**) (ΔH), (**c**) (ΔG), and (**d**) (ΔS).

In this stage, the *Ea* lies in a range of (5.16–128.78 kJ/mol), A in the range of (9.15×10^{-4}–5.32×10^{8} s^{-1}) for every reaction mechanism, and the best models are F2, F1, F1, F1, F1, and D3 with an R^2 of 0.982, 0.984, 0.990, 0.994, 0.994, and 0.995; *A* values of 3.44×10^{6} s^{-1}, 2.98×10^{2} s^{-1}, 2.22×10^{2} s^{-1}, 2.73×10^{2} s^{-1}, 2.61×10^{2} s^{-1}, and 2.36×10^{6} s^{-1}; and *Ea* values of 79.01 kJ/mol, 60.05 kJ/mol, 59.05 kJ/mol, 60.86 kJ/mol, 60.60 kJ/mol, 119.40 kJ/mol, respectively, and the (WS−WB) blends, i.e., 100WS, 80WS−20WB, 60WS−40WB, 40WS−60WB, 20WS−80WB, and 100WB, are considered the most feasible mechanism for their thermal degradation, as depicted in Figure 10a. This shows that the co-pyrolysis of 100WS reduces the *Ea* of 100WB [72]. The value of the (*A*) decreases as the ratio of WB increases and further increases with the increase in the ratio of WB. The reaction becomes more complicated as the value of *A* becomes larger [73]. The co-pyrolysis process provides an additional key aspect of thermal behavior, namely kinetic properties, that contributes to reactor design. The research discovered that kinetic features can be utilized to demonstrate the co-pyrolysis process of blends [74].

The thermodynamic properties, such as enthalpy (ΔH), entropy (ΔS), and Gibbs free energy (ΔG), are key aspects to establishing the tools of engineering for the co-pyrolysis of (WS−WB) blends as a single-stage process, with a single value for each property for all fourteen reaction mechanisms. Table S1 displays T_p, which was measured from DTG analysis, and was utilized for the measurement of these properties. The thermodynamic parameters reveal crucial data regarding biomass conversion into biofuels [75]. The reaction processes' exothermic and endothermic reactions were illustrated by enthalpy. Gibbs free energy describes the increase in the system's total energy when activated complexes are formed, and the reactants become consumed. In thermodynamic equilibrium, the hard substance was exposed to a variation of chemical and physical processes because of the low entropy values [76].

In this stage, ΔH lies in a range of (1.16–123.78 kJ/mol), ΔG in a range of (147.69–184.34 kJ/mol), and ΔS in the array of ($-$0.05–($-$0.28) kJ/mol.k). The values were positive for the first two, while for all reaction mechanisms, negative values of ΔS were observed, and the best models are those with a ΔH of 74.02 kJ/mol, 55.03 kJ/mol, 54.05 kJ/mol, 55.81 kJ/mol, 55.55 kJ/mol, and 114.06 kJ/mol; ΔG of 157.12 kJ/mol, 162.26 kJ/mol, 162.31 kJ/mol, 164.22 kJ/mol, 164.20 kJ/mol, and 180.53 kJ/mol; and ΔS of $-$0.14 kJ/mol.k, $-$0.18 kJ/mol.k, $-$0.18 kJ/mol.k, $-$0.18 kJ/mol.k, $-$0.18 kJ/mol.k, and $-$0.10 kJ/mol.k for the (WS$-$WB) blends, i.e., 100WS, 80WS$-$20WB, 60WS$-$40WB, 40WS$-$60WB, 20WS$-$80WB, and 100WB, respectively. The results are displayed in Figure 10b–d and Table S1. The positive value of ΔH indicated the whole co-pyrolysis process was endothermic, necessitating the application of external heat to transform the materials into usable bio-energy [75,77]. The ΔH trailed the identical arrangement, as with an increasing ratio of WB, the *Ea* increased but decreased again with an increasing ratio in the blends. However, the difference between *Ea* and ΔH was in the range of 4.95–5.50 kJ/mol for all the blends, demonstrating the reaction was possible to yield because of the small potential energy barrier [77,78]. A higher ΔH value implies that the degradation process necessitates more energy for breaking the reactant sample's bonds [79]. In both stages, for all four blends, ΔG is constantly positive throughout the process, showing that the reaction is complex and non-spontaneous, needing external heat to accelerate the reaction [80]. As the ratio of WB increases, the ΔG values increase for all the blends. The activated complex is distinguished by an intensively established "degree of arrangement", as shown by the formation's negative ΔS values [78]. The positive value of ΔS specified that the system's active complex was chaotic, deviating from thermodynamic equilibrium, and the negative value of ΔS indicates that the system is close to approaching thermodynamic equilibrium, representing the production of a thermal product [81].

2.5. Catalytic Co-Pyrolysis in TGA

The (80WS$-$20WB) blend's catalytic co-pyrolysis over mussel shell-derived CaO catalyst was performed in TGA. The representation of catalytic co-pyrolysis blends is demonstrated as 5% CaO, 7% CaO, and 10% CaO. Their thermal degradation behavior was investigated, as seen in Figure 11a,b. The TGA-DTG profile of the catalytic blends, i.e., 5% CaO, 7% CaO, and 10% CaO, is also categorized by a three-stage thermal reaction. The first stage for the catalytic blends lies in the range of (25–150 °C), known as the moisture removal stage; the second stage, also known as the active pyrolysis region, is where most of the devolatilization occurs in the range of (150–500 °C); and the third stage, known as the secondary pyrolysis region, is where most of the degradation of the solid residue occurs that lies in the range of (500–900 °C), as shown in Figure 11a.

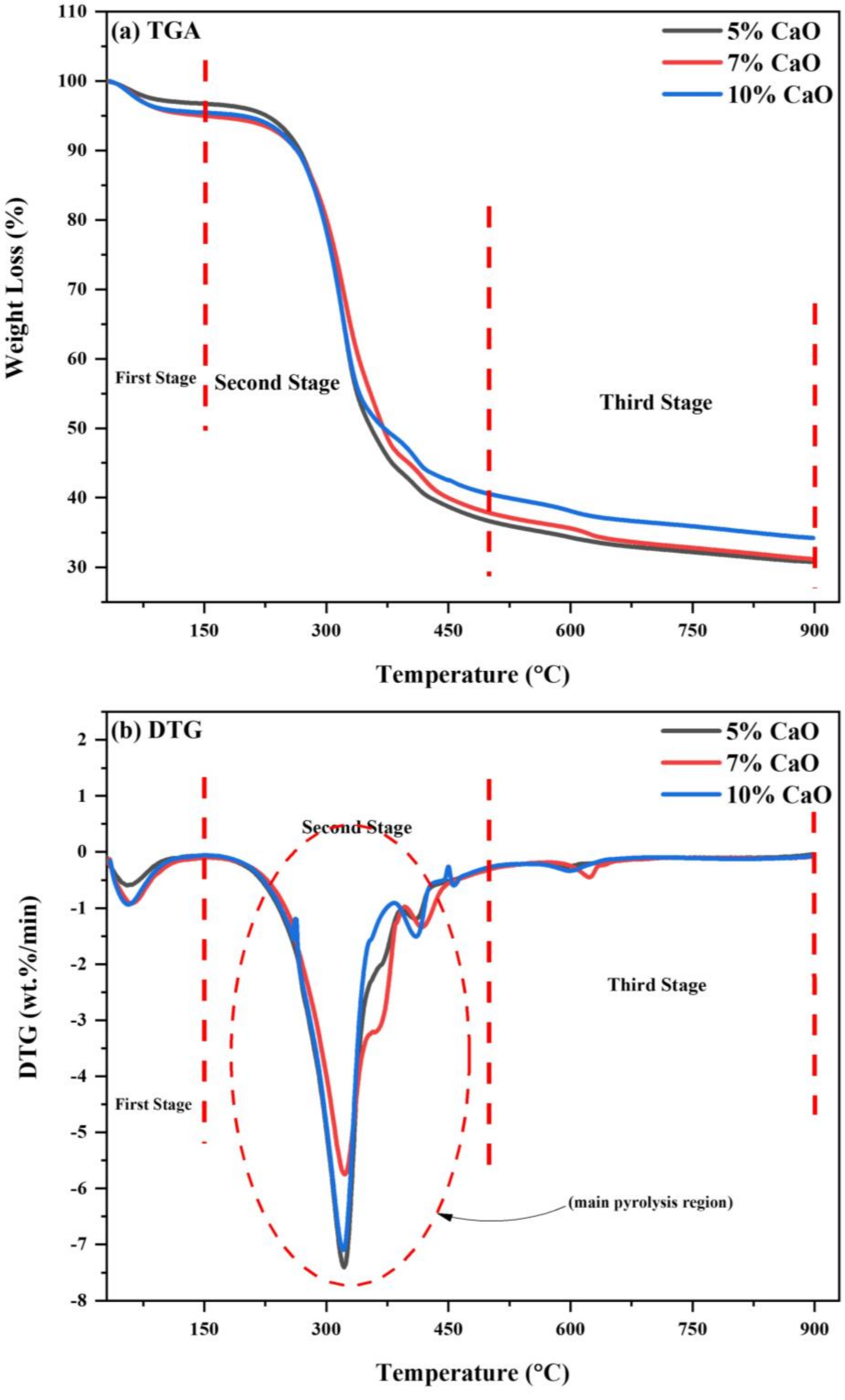

Figure 11. (**a**) TGA and (**b**) DTG curves of catalytic blends in N_2 atmosphere.

In Figure 11b, the DTG curves of the (80WS−20WB) blend with three CaO loadings are shown, demonstrating a major DTG peak in each of the three stages of the process. When we loaded mussel shell-derived CaO catalyst in three proportions, i.e., 5%, 7%, and 10%, on the optimum blend (80WS−20WB), the T_p in the first stage, at which maximum weight loss occurs, was 56.7 °C, 60.2 °C, and 56.43 °C, while the maximum degradation rate observed was −0.5871 wt.%/min, −0.9190 wt.%/min, and −0.9380 wt.%/min. This shows that in this stage, 10% CaO increased the degradation rate while slightly reducing the T_p from 56.65 °C. This stage mainly responds to the removal of watery constituents from the materials along with slightly volatile releases. During the thermal degradation in the second stage, two main peaks were observed: the first peak forms a shoulder curve-like structure, which shows the degradation of hemicellulose, followed by a primary shoulder curve at a higher temperature, which is further followed by another downward peak, so the primary shoulder, which is then followed by another prominent peak, shows the degradation of cellulose. In this stage, most of the volatiles were released at an earlier temperature in the optimum blend (80WS−20WB) with the help of the catalyst CaO, which helps in reducing the catalyst peak degradation temperature in the two loadings of 5% CaO and 10% CaO from 330.1 °C to 321.57 °C and 320.96 °C, respectively, for the first peak, thus showing prominent results. Additionally, 7% CaO loading has also lowered the temperature, but among the three loadings, it has the highest peak degradation temperature. The CaO catalyst acts as an activating agent by further lowering the peak degradation temperature [82]. The maximum degradation rate observed for 5% CaO was (−7.3974 wt.%/min) and (−1.1912 wt.%/min) at 321.57 °C and 410.34 °C; for 7% CaO, the maximum degradation rate observed was (−5.7436 wt.%/min) and (−1.3423 wt.%/min) at 322.60 °C and 417.36 °C; and for 10% CaO, it was (−7.0965 wt.%/min) and (−1.5077 wt.%/min) at 320.96 °C and 410.15 °C. Another visible peak was observed in the third stage, where the slow degradation of the solid residue takes place. In the degradation of the pure optimal blend without a catalyst, small humps were seen; this stage showed the lower range of degradation of carbon residues. However, after the addition of the catalyst, the peak also suggested the degradation of the naturally existing minerals and lignin in the later part of the catalytic co-pyrolysis process at higher temperatures. Among the three catalytic blends, 5% CaO showed the lowest degradation rate and temperature. On the other hand, the degradation rate peak of weight loss in the third stage at a temperature higher than 580 °C must be associated directly with the calcination step of $CaCO_3$, which degrades into CaO and CO_2, which leads to its decrease and appearance [83]. The maximum degradation rate observed for 5% CaO was (−0.2552 wt.%/min) at 597.25 °C; for 7% CaO, the maximum degradation rate observed was (−0.4506 wt.%/min) at 623.06 °C; and for 10% CaO, it was (−0.3346 wt.%/min) at 597.52 °C. The peak intensity of the blends varies among the catalytic blends. At the reaction's end, the overall (WL%) was 69.23%, 68.84%, and 65.80%, while the (RL%) was 30.77%, 31.16%, and 34.20% at 5% CaO, 7% CaO, and 10% CaO, respectively. The (WL%) was reduced for the optimum blend as the loading of CaO on it increased, but 5% CaO showed excellent performance results as compared to the other loadings of 7% and 10%. The catalyst's reactivity starts reducing when the percentage of the catalyst loading increases, which would favor us in only improving the biochar yield in the products, but lower catalyst loading would help in increasing the bio-oil yield effectively. However, except for CaO, none of these metal oxides, i.e., ZnO, MgO, TiO_2, NiO, and Fe_2O_3, can remove acids or create hydrocarbons [84]. CaO has a better cracking ability, which splits the carbon chain into smaller molecules without descending into the higher temperature [85]. It is claimed that employing CaO for co-pyrolysis did not generate carboxylic acids or furans since the presence of carboxylic acids would considerably reduce bio-oil output. Simultaneously, the CaO catalyst may boost the yield of ketone, phenol, alkenes, and alkadienes [86]. The maximum temperature for the reaction is restricted to 480 °C because of consequent cracking reactions above 500 °C, which will improve gas formation and also weaken bio-oil generation. It can be deduced that 5% CaO is the best catalytic blend ratio with respect to the outcome of volatiles (WL%) from TGA profiles and the breakdown rate from DTG for generating higher volatile yields in regard to bio-oil.

Thermo-Kinetic

Table S2, which provides the data for 5% CaO, 7% CaO, and 10% CaO with a 10 °C min^{-1} constant heating rate, was utilized to perform the thermodynamic and kinetic analysis obtained from TG. As discussed previously, the specified range of 0.90–0.99 was set, and fitting the data's precision relied on R^2. The fitting data accuracy was based on R^2. The main pyrolysis region for the volatile releases can be observed as the single-stage process in which the main process region lies in the overall temperature region of (150–500 °C), with individual Ea, A, R^2, ΔH, ΔG, and ΔS for all fourteen reaction mechanisms, as displayed in Figure 12a–d.

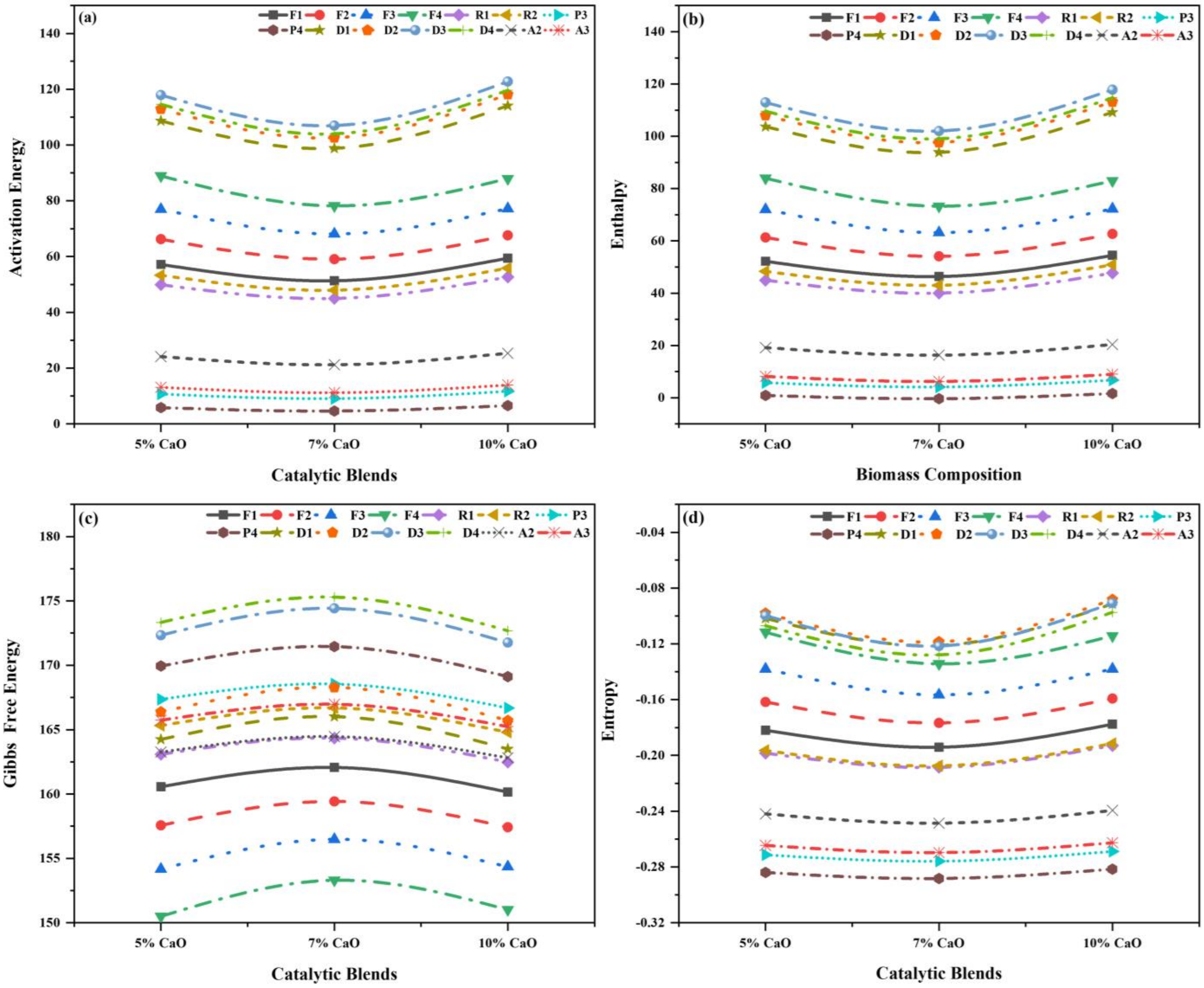

Figure 12. Thermo−kinetic properties for different models of catalytic blends: (**a**) Ea, (**b**) (ΔH), (**c**) (ΔG), and (**d**) (ΔS).

In this stage, the Ea lies in a range of (4.60–122.75 kJ/mol), A in the range of (8.33×10^{-4}–1.37×10^{7} s^{-1}) for all the reaction models, and the best models are D3, D1, and D2, with R^2 of 0.986, 0.983, and 0.986; A values of 3.49×10^{6} s^{-1}, 2.66×10^{5} s^{-1}, and 1.37×10^{7} s^{-1}; and Ea values of 117.93 kJ/mol, 98.80 kJ/mol, and 118.13 kJ/mol for the catalytic blends, i.e., 5% CaO, 7% CaO, and 10% CaO, respectively. These are considered the most possible mechanism for their thermal degradation, as depicted in Figure 12a. The Ea and A increase as the ratio of CaO increases in comparison to the non-catalytic blend, as presented in Table S2. The Ea and A of the optimum blend were observed to be lowered, to some extent, when the catalyst was added to all mass loadings.

In this stage, ΔH lies in a range of (1.65–117.81 kJ/mol), ΔG in a range of (150.49–175.29 kJ/mol), and ΔS in the range of (−0.08–(−0.288) kJ/mol.k). The values were positive for the first two, whereas the values of ΔS were negative for all the reaction mechanisms, and the best models are D3, D1, and D2, with ΔH values of 112.97 kJ/mol, 93.85 kJ/mol, and 113.18 kJ/mol; ΔG values of 172.34 kJ/mol, 166.02 kJ/mol, and 165.70 kJ/mol; and ΔS values of −0.09 kJ/mol.k, −0.12 kJ/mol.k, and −0.08 kJ/mol.k for the catalytic blends, i.e., 5% CaO, 7% CaO, and 10% CaO, respectively. The results are displayed in Figure 12b–d and Table S2. The ΔH followed the identical pattern as *Ea* increased, although the difference between *Ea* and ΔH was in the region of 4.95–5.05 kJ/mol for all the catalytic blends, indicating the reaction was likely to be generated due to a small potential energy barrier [77,78]. For *Ea*, ΔH repeated the same behavior as in the first stage; it increased for 5% CaO and then decreased at 7% CaO, while increasing again at a higher catalyst loading of 10% CaO. The values of ΔG decreased when CaO's ratio in the blends increased. The indication of complex reactions was indicated by the positive values and for speeding up the reaction, a suitable amount of external energy was required [73]. Values of ΔS that are negative show how near the system was to the attainment of thermodynamic equilibrium. Low ΔS indicates that the material has lately undergone physical or chemical aging, putting it near thermodynamic equilibrium [67,73]. Lastly, during catalytic co-pyrolysis, the best blend that improved the optimum blends (80WS−20WB) (WL%), resulting in improving the yield of bio-oil, was 5% CaO.

2.6. Significance of the Study

The significance of this study is that it helps in optimizing catalytic conditions and provides insights into how to design and choose appropriate catalysts and feedstock for specific applications, improving process efficiency and product quality. Thermogravimetric analysis (TGA)-based catalytic co-pyrolysis is a technique used to study interactions between catalysts and feedstocks during co-pyrolysis. TGA provides real-time data on weight loss as a function of temperature, allowing researchers to monitor the decomposition behavior of feedstocks in the presence of a catalyst. It helps in identifying the synergy analysis between the feedstocks and shows how their interactions modify their reaction pathways. It also helps in optimizing the temperature and catalytic conditions for co-pyrolysis processes, which leads to improved product (bio-oil, biogas, and biochar) yields and quality. Its limitation is that it is used for small-scale experiments, and results may not always scale linearly to larger industrial processes. The insights gained from such studies are crucial for improving biomass conversion processes and advancing sustainable energy technologies. Table 5 shows the catalytic co-pyrolysis literature comparison with previous studies.

Table 5. Catalytic co-pyrolysis literature comparison.

S.No	Blends with Catalyst	Catalytic Blends	Best Catalytic Blend	Reaction Condition in TGA	Activation Energy-E_a (kJ/mol)	Synergy Analysis Deviation (%)	Ref.
1.	Wheat straw biomass (WS), woody sawdust biomass (WB) using mussel shell-derived CaO catalyst	5% CaO (0.05:0.95), 7% CaO (0.07:0.93), and 10% CaO (0.10:0.90),	5% CaO	T = 25–900 °C Heating rate = 20 °C/min	117.93 kJ/mol	0.19%	Present work
2.	Corncob biomass with HDPE waste plastic using chicken and duck eggshell catalysts	Corncob:HDPE = 0.9:0.1 Corncob:HDPE:Chicken eggshell = 0.8:0.1:0.1 Corncob:HDPE:Duck eggshell = 0.8:0.1:0.1	All the catalytic blends showed better performance with chicken eggshell, which shows it as a more favorable one	T = (373 K–1173 K) 100–900 °C Heating rate = 10, 20, 50, 100, 200 K/min	59.64 kJ/mol	NR	[87]
3.	10%CeO$_2$@MNA/(20 BCE-80 AC)	3 wt% and 5 wt%	3 wt% with an increase in WL% from 45.9% to 68.7%	T = 25–900 °C Heating rate = 20 °C/min	67.82 kJ/mol	3.55%	[19]
4.	Kukersite oil shale and black pine wood with HZSM-5(23), HBETA(25), and HY(30)	(BPW/KOS: 1/1) and catalyst-to-sample weight ratio (3/1)	-	T = 25–800 °C Heating rate = 10 °C/min	22.8 kJ/mol 20.3 kJ/mol 22.2 kJ/mol	NR	[88]
5.	Cellulose, Douglas fir, and LDPE with HZSM-5	Ratio of 4:1	DF-LDPE-catalyst	T = 25–600 °C, Heating rate = 20 °C/min	54.51 kJ/mol	NR-	[89]

Table 5. *Cont.*

S.No	Blends with Catalyst	Catalytic Blends	Best Catalytic Blend	Reaction Condition in TGA	Activation Energy-E_a (kJ/mol)	Synergy Analysis Deviation (%)	Ref.
6.	Seaweeds and HDPE with HZSM-5	Ratio of 1:1:2	Seaweeds-HDPE-HZSM-5,	T = 25–800 °C, Heating rate = 10, 20, 30 and 40 °C/min	(104.21–113.78) kJ/mol	NR	[90]
7.	Spirulina and oil shale with CaO and HZSM-5	3CaO1HZSM-5 1CaO1HZSM-5 1CaO3HZSM-5	SP and OS with $1CaO_3HZSM$-5	T = 25–900 °C, Heating rate = 20 °C/min	192.53 kJ/mol	NR	[91]
8.	Empty fruit bunch (EFB) biomass and recycled (HDPE) plastic with rice husk ash (RHA) and HZSM-5 catalyst	EFB-to-HDPE mass ratio of 1:1, catalyst-to-feedstock mass ratio of 1:1 (Raw RHA, RHA-T, HZSM-5)	Rice husk ash catalyst	T = 30–700 °C Heating rate = 20 °C/min	70.04 kJ/mol	NR	[92]

3. Materials and Methodology

3.1. Material and Catalyst Preparation

3.1.1. Material Preparation

Consequently, locally sourced wheat straw (WS) and woody sawdust biomass (WB) are utilized in this research. Figure 13 represents the schematic for the preparation of WS—WB samples in which they are first dried inside an oven at a temperature of 105 °C for 1 day for the purpose of eliminating any moisture content. After that, a mixer–grinder is utilized for grinding–crushing purposes to obtain 0.2 mm particle size samples with the help of a sieve. All the blends of WS—WB were prepared on a weight % basis by mixing wheat straw (100WS) with woody sawdust biomass (100WB) to make 100% wt. of blends besides the pure samples. Thus, 80WS—20WB symbolizes that 80% wt. wheat straw was mixed with 20% wt. woody sawdust; likewise, 60WS—40WB, 40WS—60WB, and 20WS—80WB blends were prepared accordingly. By these calculations, all the samples were prepared as shown in Table 6. Pure samples of WS and WB were referred to as pure wheat straw (100WS) and pure woody sawdust (100WB), respectively.

Figure 13. Material preparation of WS-WB blends.

Table 6. Details of blend composition along with sample code.

Sample Code	Weight (%) Composition of Blends					
	100WS	**80WS−20WB**	**60WS−40WB**	**40WS−60WB**	**20WS−80WB**	**100WB**
Wheat Straw (WS)	100	80	60	40	20	0
Woody Sawdust (WB)	0	20	40	60	80	100

3.1.2. Catalyst Preparation

The CaO was prepared through the process of calcination. Waste mussel shells were cleaned by washing them several times in warm water and then drying them fully at room temperature. The dried mussel shells were calcined for 4 h in an oxygen environment at 950 °C at a heating rate of 10 °C/min using an electric furnace (Yamato Standard Electric Furnace FO 610, Yamato Scientific Co., Ltd., Tokyo, Japan) [56]. This process yielded a powder that was further sieved and crushed via a 63 µm sieve, resulting in a white powder. The schematic that explains the synthesis process of CaO catalyst obtained through the calcination of mussel shells in represented in Figure 14.

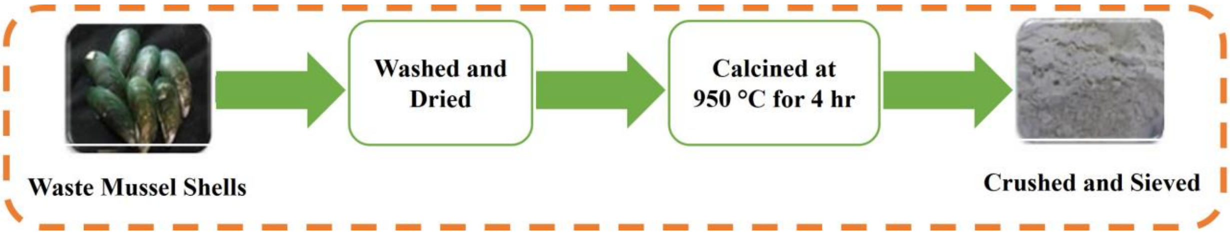

Figure 14. Catalyst preparation process of mussel shell-based catalyst.

3.2. *Catalytic Blend Preparation*

The sample was prepared for catalytic co-pyrolysis utilizing the in situ approach, where the optimal mixture and catalyst were combined directly. The mussel shell-produced CaO catalyst was immediately blended with the best blend of 100WS and 100WB. A hand mortar was then utilized for grinding purposes. To form a 2 g sample, they blended in three distinct proportions of 5 wt.%, 7 wt.%, and 10 wt.% CaO catalyst with the optimum blend. At catalyst mass loading, the new mixture was subsequently developed, and the optimum blend loading ratios of 5 wt.% (0.05:0.95), 7 wt.% (0.07:0.93), and 10 wt.% (0.10:0.90) were used. To ensure blending accuracy, a Digital GSM Balance was utilized to weigh the samples, and then a vortex mixer (F20220176, VELP SCIENTIFICA, Usmate Velate, Italy) was utilized for mixing the vial for 5 min, in which the weighed samples were placed [19].

3.3. *Characterization*

A PerkinElmer 2400 Series II CHNS/O Elemental Analyzer (PerkinElmer, Waltham, MA, USA)was utilized for the ultimate analysis to compare the percentages of C, H, N, S, and O content in pure 100WS and 100WB to the standard values. For ultimate analysis, the weight of each material loaded was in the material size range of 0 to 500 mg. The GCV analysis of pure 100WS and 100WB was performed by the customary procedure (ASTM D5865-13) and it was obtained by using a Parr 6200 oxygen bomb calorimeter. Each sample weighed 1 g.

A Bruker Alpha II Spectrometer with diamond ATR–FTIR detection was employed to record the FTIR spectra for analyzing the structural analysis of the specimens with a 4000–400 cm^{-1} wavelength range.

X-ray diffraction (XRD) analysis was done by utilizing Bruker's D8 advance X-ray Diffractometer (Bruker, Karlsruhe, Germany) with a sample scanning speed of 0.06° min^{-1} for 2θ with a range between 30° and 60°. Furthermore, for the evaluation of XRD spectra and peaks, JADE 6.0 was utilized, which incorporated a built-in Powder Diffraction File

(PDF) or Joint Committee on Powder Diffraction Standards (JCPDS) for the search and match option.

TESCAN MIRA 3 Schottky field emission scanning electron microscope (TESCAN, Brno, Czech Republic)was utilized to carry out Field Emission Scanning Electron Microscopy (FESEM), along with Energy-Dispersive X-ray spectroscopy (EDX), for performing an analysis of the morphology and structure of the elements in the specimen. The machine possesses a 10–200,000X extension for procuring magnified 2D images along with a resolution of about 2 nm. Furthermore, color mapping was also done by utilizing this microscope.

A PerkinElmer TGA 4000 thermogravimetric analyzer was used to investigate the thermal degradation behavior of (WS−WB) blends. Nitrogen gas (N_2) flow was monitored by a mass flow controller and maintained to provide an inert atmosphere for conducting the experiment. After that, at a 10 °C min^{-1} heating rate, the samples were heated to 1000 °C from 25 °C by utilizing a platinum pan. The particle size and weight of each blend loaded were 0.2 mm and 10 mg, respectively. The suitable estimation of kinetic parameters during co-pyrolysis and important information about the degradation rate and (WL%) is provided by TGA [93].

3.4. Synergy Analysis

The synergy analysis of four (WS−WB) blends is explored by the comparison of calculated and experimentally derived values from TGA/DTG. Synergy analysis is performed to analyze how the 100WS and 100WB biomasses will interact during co-pyrolysis to support their degradation. For positive synergy analysis, the experimentally derived value is greater than zero, indicating the existence of synergy analysis and the favorable impact of co-pyrolysis, and less than zero for negative synergy analysis, indicating the inhibitory impact of co-pyrolysis and denying synergy analysis existence. Thus, if the experimental values will be higher than the calculated values [94], a significantly greater synergy will be observed as a result of a greater deviation amongst experimental and calculated values [95]. The calculated values are the addition of individual samples that are directly proportional to the weight ratio of blends because the assumption that no interactions were observed throughout co-processing was made by the additive model [96,97]. Equation (4) is utilized for finding the calculated values of WS−WB blends.

$$S_C = M_{B1.mr}\left(S_{exp.B1}\right) + M_{B2.\,mr}\left(S_{exp.B2}\right) \tag{4}$$

Blended materials $M_{B1.mr}$ and $M_{B2.\,mr}$ reflect the mass ratios of 100WS and 100WB biomass, respectively. $S_{exp.B1}$ and $S_{exp.B2}$ are the experimental findings of 100WS and 100WB biomass, respectively. The residue left and weight loss are denoted as (RL%) and (WL%). The difference between the calculated and experimental values of ($(\text{DTG})_{\max}$ %), (RL%), and (WL%) was calculated by utilizing Equation (5). During co-pyrolysis of the four (WS−WB) blends, the absence or presence of synergy analysis will be highlighted by Equation (5) [64].

$$Deviation\ (\%) = \frac{S_E - S_C}{S_C} \times 100 \tag{5}$$

where the values calculated through Equation (4) are denoted by S_C, and during TGA/DTG analysis, the experimentally measured values obtained are denoted by S_E.

3.5. Thermo-Kinetic Modeling

The kinetic analysis of co-pyrolysis and catalytic co-pyrolysis is an incredibly challenging method because of the involvement of multiple intermediary and overlapped reaction processes. An important process is the conversion of (WS−WB) blends into products through co-pyrolysis and catalytic co-pyrolysis. A co-pyrolytic and catalytic co-pyrolysis kinetic investigation is valuable in the process of designing, optimizing, and operating [98]. A thermo-kinetic study of (WS−WB) blends was carried out via a model-fitting method, i.e., Coats–Redfern method, which is an old-style kinetic analysis method, thus requiring a single heating rate to estimate kinetic parameters, i.e., pre-exponential factor (A), Coefficient of Determination (R^2) and activation energy (Ea). Almost fourteen (14) reaction models, as revealed in Table 7, are used to establish them. This technique extensively utilizes models for kinetic investigation of biomasses and other materials [99], eventually demonstrating the complete degradation procedure of a material, supposing it is a standalone reaction with first-order kinetics. For co-pyrolysis and catalytic co-pyrolysis, the insight into overall volatile release kinetic was established by applying this approach to TGA [100]. The degradation of (WS−WB) blends was divided into single stages for more precise measurement of A and Ea. The measurement of kinetics parameters did not contain the moisture content stages.

Table 7. Commonly used reaction models' detailed algebraic expressions.

Symbols	**Reaction Mechanism**	**Algebraic Expressions**	
		Differential Form $f(\alpha)=\frac{1}{k}\frac{d\alpha}{dt}$	**Integral Form** $g(\alpha)=kt$
	Geometric Contraction Models		
R1	Contracting disk	1	α
R2	Contracting cylinder	$2(1-\alpha)^{\frac{1}{2}}$	$1-(1-\alpha)^{\frac{1}{2}}$
	Power Law		
P3	Power law; P3	$3(\alpha)^{\frac{2}{3}}$	$(\alpha)^{\frac{1}{3}}$
P4	Power law; P4	$4(\alpha)^{\frac{3}{4}}$	$(\alpha)^{\frac{1}{4}}$
	Reaction Order Models		
F1	First-order	$(1-\alpha)$	$-\ln(1-\alpha)$
F2	Second-order	$(1-\alpha)^2$	$(1-\alpha)^{-1}-1$
F3	Third-order	$(1-\alpha)^3$	$\frac{1}{2}\left[(1-\alpha)^{-2}-1\right]$
F4	Fourth-order	$(1-\alpha)^4$	$\frac{1}{4}\left[(1-\alpha)^{-3}-1\right]$
	Nucleation Models		
A2	Avarami–Erofe'ev for n = 2	$2\,(1-\alpha)[-\ln(1-\alpha)]^{\frac{1}{2}}$	$[-\ln(1-\alpha)]^{\frac{1}{2}}$
A3	Avarami–Erofe'ev for n = 3	$3\,(1-\alpha)[-\ln(1-\alpha)]^{\frac{1}{3}}$	$[-\ln(1-\alpha)]^{\frac{1}{3}}$
	Diffusivity Models		
D1	Parabolic law	$\frac{1}{2}\alpha$	α^2
D2	Valansi equation	$-[\ln(1-\alpha)]^{-1}$	$\alpha+[(1-\alpha)\ln(1-\alpha)]$
D3	Jander equation	$2\,(1-\alpha)^{\frac{2}{3}}\left[1-(1-\alpha)^{\frac{1}{3}}\right]^{-1}$	$\left[1-(1-\alpha)^{\frac{1}{3}}\right]^2$
D4	Ginstling Brounstein equation	$\frac{3}{2}\left[(1-\alpha)^{-\frac{1}{3}}-1\right]^{-1}$	$1-\frac{2}{3}\alpha-(1-\alpha)^{\frac{2}{3}}$

To understand the kinetics' mechanism, the formulation of a solid-state reaction kinetic equation is first done and solved. Equation (6) represents a single reaction that can describe the thermal degradation of (WS−WB) blends:

$$\text{Biomass}_{(\text{solid})} \rightarrow \text{Biochar}_{(\text{solid})} + \text{Volatile releases}_{(\text{liquid+gas})} \tag{6}$$

Equation (7) represents solid-state reaction's rate equation:

$$\frac{d\alpha}{dt} = k(T)\cdot f(\alpha) \tag{7}$$

In Equation (7), the reaction mechanism is denoted as $f(\alpha)$, which, having n as the order of reaction, is further expressed as $(1-\alpha)^n$, the rate constant is denoted by *k(T)*, and the conversion rate is represented as α, having its value lie in the (0–1) range. The weight of the sample is calculated continuously as a function of time and temperature during the TGA/DTG experiment. By using the weight range, during co-pyrolysis and catalytic co-pyrolysis, the conversion rate (α) at any time (t) is measured using Equation (8):

$$\alpha = \frac{weight_i - weight_{ins}}{weight_i - weight_f} \tag{8}$$

where the beginning weight of the material before going through degradation (g) is denoted as weight_i, the spontaneous weight of the material at time t (g) is represented as weight_ins, and the final weight of the material after degradation (g) is denoted by weight_f. The heating rate is expressed as ($\beta = \frac{dT}{dt}$), where dt represents the derivative of time while dT is the derivative of temperature. Moreover, the Arrhenius equation could be utilized to measure the rate constant k. It is given in Equation (9):

$$k(T) = A \cdot exp\left(-\frac{Ea}{RT}\right) \tag{9}$$

In Equation (9), $k(T)$ is termed as the rate constant, the absolute temperature is represented by T in Kelvin, the universal gas constant is termed as R (8.314 $\text{J.K}^{-1}.\text{mol}^{-1}$), the pre-exponential factor is termed as A in s^{-1}, and activation energy is given as Ea in kJ mol^{-1}. The rate of a reaction is known as the differential of conversion concerning time. With temperature dependence from Arrhenius law under a constant heating rate β, adding in Equation (9) in Equation (7), and thus assuming $n = 1$, the fundamental Arrhenius rate expression can be reorganized in the form of Equation (10):

$$\frac{d\alpha}{dT} = \frac{A}{\beta} \cdot exp\left(-\frac{Ea}{RT}\right) \cdot (1-\alpha) \tag{10}$$

Fuel pyrolysis is often termed a first-order reaction, being completely related to degradation reactions in many applications. Equation (11) is obtained as a result of the integration of Equation (10).

$$g(\alpha) = \int_0^\alpha \frac{d\alpha}{f(\alpha)} = \frac{A}{\beta} \int_{T_0}^{T} exp\left(-\frac{Ea}{RT}\right) dT \tag{11}$$

In Equation (7), the reaction model's integrated form is denoted as $g(\alpha)$. Equation (12) is a result of Taylor expansion utilized by the Coats–Redfern integral method in Equation (11):

$$ln\left[\frac{g(\alpha)}{T^2}\right] = ln\left[\frac{AR}{\beta Ea}\left(1 - \frac{2RT}{Ea}\right)\right] - \frac{Ea}{RT} \tag{12}$$

where $\left(1 - \frac{2RT}{Ea}\right)$ is negligible and is thus removed from Equation (12). For a first-order reaction, $g(\alpha) = -ln(1-\alpha)$, as presented in Equation (13) and Equation (14), respectively [101].

$$ln\left[\frac{g(\alpha)}{T^2}\right] = ln\left[\frac{AR}{\beta Ea}\right] - \frac{Ea}{RT} \tag{13}$$

$$ln\left[\frac{-ln(1-\alpha)}{T^2}\right] = ln\left[\frac{AR}{\beta Ea}\right] - \frac{Ea}{RT} \tag{14}$$

The slope of the line results in activation energy Ea, and by drawing a graphical curve between $\frac{1}{T}$ and $ln\left[\frac{-ln(1-\alpha)}{T^2}\right]$, its intercept results in pre-exponential factor A. A linear line is obtained for this plot at n=1 [102]. ($y = mx + c$) resembles the form of Equation (14).

The parameters $y,\ x$ show $y\ axis = ln\left[\frac{g(\alpha)}{T^2}\right]$ and $x\ axis = \frac{1}{T}$, and $m = \frac{Ea}{R}$ and $c = ln\left[\frac{AR}{\beta Ea}\right]$ show (slope) and (intercept) [103,104]. The pre-exponential factor value is calculated from intercept $A = \frac{exp(c)\ \beta Ea}{R}$. The Coats–Redfern integral method was utilized using common reaction models, namely $f(\alpha)$ and $g(\alpha)$, which are represented in Table 7 [105–107]. At a specific stage, its data for reaction kinetics of weight loss are calculated by the most fitting model of $g(\alpha)$ with the highest R^2.

The Coats–Redfern integral method provided the *Ea* values via analysis of the kinetic parameters, which were then utilized to calculate ΔS, ΔH, and ΔG, which are termed as changes in entropy, enthalpy, and Gibbs free energy, respectively. In a reversible process, the highest amount of work that a closed system can produce is defined as Gibbs free energy. At constant pressure during a chemical reaction, the total heat transferred is termed enthalpy. The randomness in any system is termed entropy [79]. The thermodynamic properties' calculations are estimated using Equations (15)–(17), given below [80]:

$$\Delta H = Ea - R \cdot T_p \tag{15}$$

$$\Delta G = \mathrm{Ea} + R \cdot T_p\ \ ln\left(\frac{k_b T_p}{hA}\right) \tag{16}$$

$$\Delta S = \frac{\Delta H - \Delta G}{T_p} \tag{17}$$

where the DTG peak degradation temperature is represented as T_p in K (Kelvin), the Planck constant is represented by h with the value of 6.63×10^{-34} Js, the universal gas constant is denoted as R, and the Boltzmann constant (1.38×10^{-23} J/K) is denoted by k_b.

3.6. Catalytic Co-Pyrolysis in TGA

The optimal blend was utilized with the catalyst in a PerkinElmer TGA 4000, a thermogravimetric analyzer, to carry out the catalytic co-pyrolysis. In the first step, the samples were purged for half an hour with N_2 and then placed inside a crucible pan made of platinum. After that, the samples weighing 10 mg were heated in an inert environment at a rate of 10 °C/min from 25 to 900 °C [19].

4. Conclusions

The co-pyrolysis behavior of wheat straw (WS) and woody sawdust biomass (WB) was studied in detail in this research. Various blending ratios, along with pure raw materials, were characterized by TGA, CHNS-O, and GCV. CaO was characterized via XRD, SEM, EDX, and FTIR for structural, morphological, and elemental analysis. Their thermal characteristics were studied by carrying out co-pyrolysis in TGA with 10 °C/min as the heating rate. These results formulated the evaluation of the synergy analysis of all samples. The co-pyrolysis of WS with WB outclasses the pyrolysis of single materials in regard to reducing the activation energy and showing better synergy analysis results for the optimum blend, i.e., 80WS−20WB, with a positive deviation of 0.19% in terms of (WL%) predicting good results for bio-oil production. The F1 model served as the best model that describes the *Ea* of 60.05 kJ/mol and the ΔH, ΔG, and ΔS values of 55.03 kJ/mol, 162.26 kJ/mol, and −0.18 kJ/mol.K, respectively for the best blend 80WS−20WB. Thermodynamic properties (ΔH, ΔG, and ΔS) reciprocate viability, spontaneity, and steady product formation in co-pyrolysis. Catalytic co-pyrolysis was carried out using CaO as a catalyst to study its effects on production yield. Through catalytic co-pyrolysis, 5% CaO was the best mixture, increasing the (WL%) of the ideal blend (80WS−20WB). Therefore, D3 served as the best model for 5% CaO that describes the *Ea* of 117.93 kJ/mol and ΔH, ΔG, and ΔS values of 112.97 kJ/mol, 172.34 kJ/mol, and $-0.09\ \frac{\mathrm{kJ}}{\mathrm{mol}}$.k, respectively, thus boosting its bio-oil output. Gained results are critical for the effective design and modeling of catalytic co-pyrolysis systems of (WS−WB) blends and in scaling up industrial biomass conversion applications.

Supplementary Materials: The following supporting information can be downloaded at: https://www.mdpi.com/article/10.3390/catal14090655/s1, Table S1: Represents the Thermo-Kinetic Properties of (WS-WB) blends, Table S2: Represents the Thermo-Kinetic properties of the Optimum Blend with three mass loadings.

Author Contributions: M.S.: Conceptualization, Methodology, Investigation, Data curation, and Writing—Original Draft. A.B.: Methodology and Investigation, Writing—Original Draft, Writing—Review and Editing, and Project Administration. All authors have read and agreed to the published version of the manuscript.

Funding: This research work was funded by Institutional Fund Projects under grant no. (IFPIP: 443-829-1443). The authors gratefully acknowledge the technical and financial support provided by the Ministry of Education and King Abdulaziz University, DSR, Jeddah, Saudi Arabia.

Data Availability Statement: The original contributions presented in the study are included in the article/Supplementary Material; further inquiries can be directed to the corresponding author.

Conflicts of Interest: The authors declare no conflicts of interest.

Nomenclature

A	Pre-exponential factor
CaO	Calcium oxide
CHNS-O	Carbon, Hydrogen, Nitrogen, Sulfur, and Oxygen
DTG	Derivative thermogravimetry
Ea	Activation energy
K	Rate constant
FTIR	Fourier transform infrared spectroscopy
h	Planck constant
GCV	Gross Calorific Value
$\mathbf{R^2}$	Coefficient of Determination
TGA	Thermogravimetric analysis
R	Gas constant
SEM-EDS	Scanning Electron Microscopy and Energy Dispersive Spectroscopy
SRWC	Short-rotation-woody-crops
(WL%)	Weight loss %
100WS	Wheat straw
(RL%)	Residue left %
100WB	Woody sawdust biomass
WS-WB	Wheat straw and woody sawdust biomass
XRD	X-ray diffraction
$\boldsymbol{\beta}$	Heating rate
$\boldsymbol{\alpha}$	Conversion Factor
$\mathbf{\Delta H}$	Enthalpy
$\mathbf{\Delta S}$	Entropy
$\mathbf{\Delta G}$	Gibbs free energy
$\mathbf{k_b}$	Boltzmann constant
$\mathbf{f(\alpha)}$	Reaction mechanism
$\mathbf{g(\alpha)}$	Integral Function
$\mathbf{T_p}$	Peak degradation temperature
(wt.%/min)	Rate of weight loss % per min

References

1. Khalid, U.; Khoja, A.H.; Daood, S.S.; Khan, W.U.H.; Din, I.U.; Al-Anazi, A.; Petrillo, A. Experimental and numerical techniques to evaluate coal/biomass fly ash blend characteristics and potentials. *Sci. Total Environ.* **2024**, *912*, 169218. [CrossRef] [PubMed]
2. Khan, L.A.; Liaquat, R.; Aman, M.; Kanan, M.; Saleem, M.; Khoja, A.H.; Bahadar, A.; Khan, W.U.H. Investigation of Novel Transition Metal Loaded Hydrochar Catalyst Synthesized from Waste Biomass (Rice Husk) and Its Application in Biodiesel Production Using Waste Cooking Oil (WCO). *Sustainability* **2024**, *16*, 7275. [CrossRef]
3. IEA. *World Energy Outlook 2022*; IEA: Paris, France, 2022.

4. Lee, J.; Kim, S.; You, S.; Park, Y.-K. Bioenergy generation from thermochemical conversion of lignocellulosic biomass-based integrated renewable energy systems. *Renew. Sustain. Energy Rev.* **2023**, *178*, 113240. [CrossRef]
5. Gohar, H.; Khoja, A.H.; Ansari, A.A.; Naqvi, S.R.; Liaquat, R.; Hassan, M.; Hasni, K.; Qazi, U.Y.; Ali, I. Investigating the characterisation; kinetic mechanism, and thermodynamic behaviour of coal-biomass blends in co-pyrolysis process. *Process Saf. Environ. Prot.* **2022**, *163*, 645–658. [CrossRef]
6. Ong, H.C.; Chen, W.-H.; Singh, Y.; Gan, Y.Y.; Chen, C.-Y.; Show, P.L. A state-of-the-art review on thermochemical conversion of biomass for biofuel production: A TG-FTIR approach. *Energy Convers. Manag.* **2020**, *209*, 112634. [CrossRef]
7. Singh, R.K.; Patil, T.; Pandey, D.; Tekade, S.P.; Sawarkar, A.N. Co-pyrolysis of petroleum coke and banana leaves biomass: Kinetics, reaction mechanism, and thermodynamic analysis. *J. Environ. Manag.* **2022**, *301*, 113854. [CrossRef] [PubMed]
8. Picchio, R.; Latterini, F.; Venanzi, R.; Stefanoni, W.; Suardi, A.; Tocci, D.; Pari, L. Pellet production from woody and non-woody feedstocks: A review on biomass quality evaluation. *Energies* **2020**, *13*, 2937. [CrossRef]
9. Stolarski, M.J.; Stachowicz, P.; Dudziec, P. Wood pellet quality depending on dendromass species. *Renew. Energy* **2022**, *199*, 498–508. [CrossRef]
10. Ahmed, A.; Bakar, M.S.A.; Sukri, R.S.; Hussain, M.; Farooq, A.; Moogi, S.; Park, Y.-K. Sawdust pyrolysis from the furniture industry in an auger pyrolysis reactor system for biochar and bio-oil production. *Energy Convers. Manag.* **2020**, *226*, 113502. [CrossRef]
11. Wang, S.; Song, T.; Yin, S.; Hartge, E.-U.; Dymala, T.; Shen, L.; Heinrich, S.; Werther, J. Syngas, tar and char behavior in chemical looping gasification of sawdust pellet in fluidized bed. *Fuel* **2020**, *270*, 117464. [CrossRef]
12. Taghizadeh-Alisaraei, A.; Tatari, A.; Khanali, M.; Keshavarzi, M. Potential of biofuels production from wheat straw biomass, current achievements and perspectives: A review. *Biofuels* **2023**, *14*, 79–92. [CrossRef]
13. Gupta, S.; Mondal, P. Catalytic pyrolysis of pine needles with nickel doped gamma-alumina: Reaction kinetics, mechanism, thermodynamics and products analysis. *J. Clean. Prod.* **2021**, *286*, 124930. [CrossRef]
14. Biswas, B.; Kumar, A.A.; Bisht, Y.; Singh, R.; Kumar, J.; Bhaskar, T. Effects of temperature and solvent on hydrothermal liquefaction of Sargassum tenerrimum algae. *Bioresour. Technol.* **2017**, *242*, 344–350. [CrossRef]
15. El-Sayed, S.A.; Mostafa, M.E. Pyrolysis and co-pyrolysis of Egyptian olive pomace, sawdust, and their blends: Thermal decomposition, kinetics, synergistic effect, and thermodynamic analysis. *J. Clean. Prod.* **2023**, *401*, 136772. [CrossRef]
16. Gouws, S.M.; Carrier, M.; Bunt, J.R.; Neomagus, H.W. Co-pyrolysis of torrefied biomass and coal: Effect of pressure on synergistic reactions. *J. Anal. Appl. Pyrolysis* **2022**, *161*, 105363. [CrossRef]
17. Mariyam, S.; Zuhara, S.; Parthasarathy, P.; McKay, G. A Review on Catalytic Fast Co-Pyrolysis Using Analytical Py-GC/MS. *Molecules* **2023**, *28*, 2313. [CrossRef] [PubMed]
18. Nandakumar, T.; Dwivedi, U.; Pant, K.K.; Kumar, S.; Balaraman, E. Wheat straw/HDPE co-reaction synergy and enriched production of aromatics and light olefins via catalytic co-pyrolysis over Mn, Ni, and Zn metal modified HZSM-5. *Catal. Today* **2023**, *408*, 111–126. [CrossRef]
19. Khan, W.U.H.; Khoja, A.H.; Gohar, H.; Naqvi, S.R.; Din, I.U.; Lumbers, B.; Salem, M.A.; Alzahrani, A.Y. In depth thermokinetic investigation on Co-pyrolysis of low-rank coal and algae consortium blends over CeO_2 loaded hydrotalcite (MgNiAl) catalyst. *J. Environ. Chem. Eng.* **2022**, *10*, 108293. [CrossRef]
20. Shafaghat, H.; Lee, H.W.; Tsang, Y.F.; Oh, D.; Jae, J.; Jung, S.-C.; Ko, C.H.; Lam, S.S.; Park, Y.-K. In-situ and ex-situ catalytic pyrolysis/co-pyrolysis of empty fruit bunches using mesostructured aluminosilicate catalysts. *Chem. Eng. J.* **2019**, *366*, 330–338. [CrossRef]
21. Lee, X.J.; Ong, H.C.; Gan, Y.Y.; Chen, W.-H.; Mahlia, T.M.I. State of art review on conventional and advanced pyrolysis of macroalgae and microalgae for biochar, bio-oil and bio-syngas production. *Energy Convers. Manag.* **2020**, *210*, 112707. [CrossRef]
22. Das, P.; Chandramohan, V.; Mathimani, T.; Pugazhendhi, A. Recent advances in thermochemical methods for the conversion of algal biomass to energy. *Sci. Total Environ.* **2021**, *766*, 144608. [CrossRef] [PubMed]
23. Xu, T.; Xu, J.; Wu, Y. Hydrogen-rich gas production from two-stage catalytic pyrolysis of pine sawdust with calcined dolomite. *Catalysts* **2022**, *12*, 131. [CrossRef]
24. Jin, X.; Lee, J.H.; Choi, J.W. Catalytic co-pyrolysis of woody biomass with waste plastics: Effects of HZSM-5 and pyrolysis temperature on producing high-value pyrolytic products and reducing wax formation. *Energy* **2022**, *239*, 121739. [CrossRef]
25. Wang, W.; Li, X.; Ye, D.; Cai, L.; Shi, S.Q. Catalytic pyrolysis of larch sawdust for phenol-rich bio-oil using different catalysts. *Renew. Energy* **2018**, *121*, 146–152. [CrossRef]
26. Lu, Q.; Chen, X.; Li, K.; Meng, L.; Xie, X.; Yuan, S.; Gao, Y.; Zhou, X. Synergistic effect of volatile inherent minerals on catalytic pyrolysis of wheat straw over a Fe–Ca–Ni catalyst. *Energy* **2022**, *253*, 124216. [CrossRef]
27. Zhang, H.; Luo, B.; Wu, K.; Zhao, B.; Yu, J.; Wang, S.; Tao, Y. Ex-situ catalytic pyrolysis of lignin using lignin-carbon catalyst combined with HZSM-5 to improve the yield of high-quality liquid fuels. *Fuel* **2022**, *318*, 123635. [CrossRef]
28. Burra, K.; Gupta, A. Kinetics of synergistic effects in co-pyrolysis of biomass with plastic wastes. *Appl. Energy* **2018**, *220*, 408–418. [CrossRef]
29. Seo, M.W.; Lee, S.H.; Nam, H.; Lee, D.; Tokmurzin, D.; Wang, S.; Park, Y.-K. Recent advances of thermochemical conversion processes for biorefinery. *Bioresour. Technol.* **2022**, *343*, 126109. [CrossRef]
30. Xu, J.; Niu, C.-Y.; Zhang, D.-Y.; Gen, Y.-H.; Hou, Q.-M.; Xie, Y.-H.; Bappi, P. Co-pyrolysis of rice straw and water hyacinth: Characterization of products, yields and biomass interaction effect. *Biomass Bioenergy* **2019**, *127*, 105281.

31. Mohadesi, M.; Aghel, B.; Gouran, A.; Razmehgir, M.H. Transesterification of waste cooking oil using Clay/CaO as a solid base catalyst. *Energy* **2022**, *242*, 122536. [CrossRef]
32. Zhang, S.; Xiong, J.; Lu, J.; Zhou, N.; Li, H.; Cui, X.; Zhang, Q.; Liu, Y.; Ruan, R.; Wang, Y. Synthesis of CaO from waste shells for microwave-assisted catalytic pyrolysis of waste cooking oil to produce aromatic-rich bio-oil. *Sci. Total Environ.* **2022**, *827*, 154186. [CrossRef] [PubMed]
33. Xue, X.; Zhang, C.; Xia, D.; Wang, Y.; Liang, J.; Sun, Y. Dual-catalyst catalytic pyrolysis of poplar sawdust: A systematic study on first-layered catalysts. *Chem. Eng. J.* **2022**, *431*, 134251. [CrossRef]
34. Dzol, M.A.A.M.; Balasundram, V.; Shameli, K.; Ibrahim, N.; Manan, Z.A.; Isha, R. Catalytic pyrolysis of high-density polyethylene over nickel-waste chicken eggshell/HZSM-5. *J. Environ. Manag.* **2022**, *324*, 116392. [CrossRef] [PubMed]
35. Chen, M.; Zhang, S.; Su, Y.; Niu, X.; Zhu, S.; Liu, X. Catalytic co-pyrolysis of food waste digestate and corn husk with CaO catalyst for upgrading bio-oil. *Renew. Energy* **2022**, *186*, 105–114. [CrossRef]
36. Weng, J.; Cheng, Z.; Zhang, Y.; Jiang, C.; Long, L.; Wang, J.; Pan, J. Online evaluation of catalytic co-pyrolysis of hemicellulose and polypropylene over CaO catalyst. *Fuel* **2023**, *332*, 125993. [CrossRef]
37. Vassilev, S.V.; Vassileva, C.G.; Vassilev, V.S. Advantages and disadvantages of composition and properties of biomass in comparison with coal: An overview. *Fuel* **2015**, *158*, 330–350. [CrossRef]
38. Aqsha, A.; Tijani, M.M.; Moghtaderi, B.; Mahinpey, N. Catalytic pyrolysis of straw biomasses (wheat, flax, oat and barley) and the comparison of their product yields. *J. Anal. Appl. Pyrolysis* **2017**, *125*, 201–208. [CrossRef]
39. Obernberger, I.; Thek, G. Physical characterisation and chemical composition of densified biomass fuels with regard to their combustion behaviour. *Biomass Bioenergy* **2004**, *27*, 653–669. [CrossRef]
40. Lateef, H.U.; Kazmi, M.; Tabish, A.N.; Cheema, I.I.; Rashid, M.I. Effect of demineralization on physiochemical and thermal characteristics of wheat straw. *Energy Sources Part A Recovery Util. Environ. Eff.* **2020**, 1–10. [CrossRef]
41. Zhang, C.; Li, S.; Ouyang, S.; Tsang, C.-W.; Xiong, D.; Yang, K.; Zhou, Y.; Xiao, Y. Co-pyrolysis characteristics of camellia oleifera shell and coal in a TGA and a fixed-bed reactor. *J. Anal. Appl. Pyrolysis* **2021**, *155*, 105035. [CrossRef]
42. Dhar, S.A.; Sakib, T.U.; Hilary, L.N. Biorefinery, Effects of pyrolysis temperature on production and physicochemical characterization of biochar derived from coconut fiber biomass through slow pyrolysis process. *Biomass Convers. Biorefinery* **2022**, *12*, 2631–2647. [CrossRef]
43. Channiwala, S.A.; Parikh, P.P. A unified correlation for estimating HHV of solid, liquid and gaseous fuels. *Fuel* **2002**, *81*, 1051–1063. [CrossRef]
44. Iftikhar, M.; Asghar, A.; Ramzan, N.; Sajjadi, B.; Chen, W.-Y. Biomass densification: Effect of cow dung on the physicochemical properties of wheat straw and rice husk based biomass pellets. *Biomass Bioenergy* **2019**, *122*, 1–16. [CrossRef]
45. Rajinipriya, M.; Nagalakshmaiah, M.; Astruc, J.; Robert, M.; Elkoun, S. Single stage purification of flax, hemp, and milkweed stem and their physical and morphological properties. *Int. J. Polym. Anal. Charact.* **2018**, *23*, 78–88. [CrossRef]
46. Bhattacharyya, M.; Shadangi, K.P.; Mahanta, P.; Mohanty, K. Co-pyrolysis of coal-biomass: Study on reaction kinetics and thermodynamics. *Biofuels Bioprod. Biorefining* **2022**, *16*, 725–742. [CrossRef]
47. Dai, L.; He, C.; Wang, Y.; Liu, Y.; Ruan, R.; Yu, Z.; Zhou, Y.; Duan, D.; Fan, L.; Zhao, Y. Hydrothermal pretreatment of bamboo sawdust using microwave irradiation. *Bioresour. Technol.* **2018**, *247*, 234–241. [CrossRef]
48. Cholapandian, K.; Gurunathan, B.; Rajendran, N. Investigation of CaO nanocatalyst synthesized from Acalypha indica leaves and its application in biodiesel production using waste cooking oil. *Fuel* **2022**, *312*, 122958. [CrossRef]
49. Jitjamnong, J.; Luengnaruemitchai, A.; Samanwonga, N.; Chuaykarn, N. Biodiesel production from canola oil and methanol using Ba impregnated calcium oxide with microwave irradiation-assistance. *Chiang Mai J. Sci.* **2019**, *46*, 987–1000.
50. Sari, E.P.; Wijaya, K.; Trisunaryanti, W.; Syoufian, A.; Hasanudin, H.; Saputri, W.D. The effective combination of zirconia superacid and zirconia-impregnated CaO in biodiesel manufacturing: Utilization of used coconut cooking oil (UCCO). *Int. J. Energy Environ. Eng.* **2022**, *13*, 967–978. [CrossRef]
51. Arana, J.T.; Torres, J.J.; Acevedo, D.F.; Illanes, C.O.; Ochoa, N.A.; Pagliero, C.L. One-Step Synthesis of CaO-ZnO Efficient Catalyst for Biodiesel Production. *Int. J. Chem. Eng.* **2019**, *2019*, 1806017.
52. Smith, B.C. *Infrared Spectral Interpretation: A Systematic Approach*; CRC Press: Boca Raton, FL, USA, 2018.
53. Griffiths, P.R. Fourier transform infrared spectrometry. *Science* **1983**, *222*, 297–302. [CrossRef] [PubMed]
54. Maache, A.; Chergui, A.; Djouadi, D.; Benhaoua, B.; Chelouche, A.; Boudissa, M. Effect of La doping on ZnO thin films physical properties: Correlation between strain and morphology. *Optik* **2019**, *180*, 1018–1026. [CrossRef]
55. Ahmed, N.; Iqbal, M.A.; Khan, Z.S.; Qayyum, A.A. DC Magnetron-Sputtered Mo Thin Films with High Adhesion, Conductivity and Reflectance. *J. Electron. Mater.* **2020**, *49*, 4221–4230. [CrossRef]
56. Khan, S.G.; Hassan, M.; Anwar, M.; Zeshan; Khan, U.M.; Zhao, C. Mussel shell based CaO nano-catalyst doped with praseodymium to enhance biodiesel production from castor oil. *Fuel* **2022**, *330*, 125480. [CrossRef]
57. Klug, H.P.; Alexander, L.E. *X-ray Diffraction Procedures: For Polycrystalline and Amorphous Materials*; Wiley: New York, NY, USA, 1974.
58. Goldstein, J.I.; Newbury, D.E.; Michael, J.R.; Ritchie, N.W.; Scott, J.H.J.; Joy, D.C. *Scanning Electron Microscopy and X-ray Microanalysis*; Springer: New York, NY, USA, 2017.
59. Atkins, P. *Shriver and Atkins' Inorganic Chemistry*; Oxford University Press: Oxford, NY, USA, 2010.

60. Adewole, B.Z.; Adeboye, B.S.; Malomo, B.O.; Obayopo, S.O.; Mamuru, S.A.; Asere, A.A. CO-pyrolysis of bituminous coal and coconut shell blends via thermogravimetric analysis. *Energy Sources Part A Recovery Util. Environ. Eff.* **2020**, 1–14. [CrossRef]
61. Han, B.; Chen, Y.; Wu, Y.; Hua, D.; Chen, Z.; Feng, W.; Yang, M.; Xie, Q. Co-pyrolysis behaviors and kinetics of plastics–biomass blends through thermogravimetric analysis. *J. Therm. Anal. Calorim.* **2014**, *115*, 227–235. [CrossRef]
62. Carpio, R.B.; Zhang, Y.; Kuo, C.-T.; Chen, W.-T.; Schideman, L.C.; de Leon, R.L. Characterization and thermal decomposition of demineralized wastewater algae biomass. *Algal Res.* **2019**, *38*, 101399. [CrossRef]
63. Idris, S.S.; Rahman, N.A.; Ismail, K.; Alias, A.B.; Rashid, Z.A.; Aris, M.J. Investigation on thermochemical behaviour of low rank Malaysian coal, oil palm biomass and their blends during pyrolysis via thermogravimetric analysis (TGA). *Bioresour. Technol.* **2010**, *101*, 4584–4592. [CrossRef]
64. Alam, M.; Bhavanam, A.; Jana, A.; Viroja, J.K.S.; Peela, N.R. Co-pyrolysis of bamboo sawdust and plastic: Synergistic effects and kinetics. *Renew. Energy* **2020**, *149*, 1133–1145. [CrossRef]
65. Vhathvarothai, N.; Ness, J.; Yu, Q.J. An investigation of thermal behaviour of biomass and coal during copyrolysis using thermogravimetric analysis. *Int. J. Energy Res.* **2014**, *38*, 1145–1154. [CrossRef]
66. Yang, Z.; Wu, Y.; Zhang, Z.; Li, H.; Li, X.; Egorov, R.I.; Strizhak, P.A.; Gao, X. Recent advances in co-thermochemical conversions of biomass with fossil fuels focusing on the synergistic effects. *Renew. Sustain. Energy Rev.* **2019**, *103*, 384–398. [CrossRef]
67. Merdun, H.; Laougé, Z.B. Kinetic and thermodynamic analyses during co-pyrolysis of greenhouse wastes and coal by TGA. *Renew. Energy* **2021**, *163*, 453–464. [CrossRef]
68. Hameed, Z.; Aman, Z.; Naqvi, S.R.; Tariq, R.; Ali, I.; Makki, A.A. Kinetic and Thermodynamic Analyses of Sugar Cane Bagasse and Sewage Sludge Co-pyrolysis Process. *Energy Fuels* **2018**, *32*, 9551–9558. [CrossRef]
69. Uzoejinwa, B.B.; He, X.; Wang, S.; Abomohra, A.E.-F.; Hu, Y.; He, Z.; Wang, Q. Co-pyrolysis of seaweeds with waste plastics: Modeling and simulation of effects of co-pyrolysis parameters on yields, and optimization studies for maximum yield of enhanced biofuels. *Energy Sources Part A: Recovery Util. Environ. Eff.* **2020**, *42*, 954–978. [CrossRef]
70. Naqvi, S.R.; Hameed, Z.; Tariq, R.; Taqvi, S.A.; Ali, I.; Niazi, M.B.K.; Noor, T.; Hussain, A.; Iqbal, N.; Shahbaz, M. Synergistic effect on co-pyrolysis of rice husk and sewage sludge by thermal behavior, kinetics, thermodynamic parameters and artificial neural network. *Waste Manag.* **2019**, *85*, 131–140. [CrossRef]
71. Naqvi, S.R.; Ali, I.; Nasir, S.; Taqvi, S.A.A.; Atabani, A.; Chen, W.-H. Assessment of agro-industrial residues for bioenergy potential by investigating thermo-kinetic behavior in a slow pyrolysis process. *Fuel* **2020**, *278*, 118259. [CrossRef]
72. Qi, P.; Chang, G.; Wang, H.; Zhang, X.; Guo, Q. Production of aromatic hydrocarbons by catalytic co-pyrolysis of microalgae and polypropylene using HZSM-5. *J. Anal. Appl. Pyrolysis* **2018**, *136*, 178–185. [CrossRef]
73. Ming, X.; Xu, F.; Jiang, Y.; Zong, P.; Wang, B.; Li, J.; Qiao, Y.; Tian, Y. Thermal degradation of food waste by TG-FTIR and Py-GC/MS: Pyrolysis behaviors, products, kinetic and thermodynamic analysis. *J. Clean. Prod.* **2020**, *244*, 118713. [CrossRef]
74. Gao, W.; Chen, K.; Zeng, J.; Xu, J.; Wang, B. Thermal pyrolysis characteristics of macroalgae Cladophora glomerata. *Bioresour. Technol.* **2017**, *243*, 212–217. [CrossRef]
75. Badshah, S.L.; Shah, Z.; Alves, J.L.F.; da Silva, J.C.G.; Iqbal, A. Pyrolysis of the freshwater macroalgae Spirogyra crassa: Evaluating its bioenergy potential using kinetic triplet and thermodynamic parameters. *Renew. Energy* **2021**, *179*, 1169–1178. [CrossRef]
76. Saeed, S.; Saleem, M.; Durrani, A.; Haider, J.; Riaz, M.; Saeed, S.; Qyyum, M.A.; Nizami, A.-S.; Rehan, M.; Lee, M. Determination of Kinetic and Thermodynamic Parameters of Pyrolysis of Coal and Sugarcane Bagasse Blends Pretreated by Ionic Liquid: A Step towards Optimization of Energy Systems. *Energies* **2021**, *14*, 2544. [CrossRef]
77. Badshah, S.L.; Shah, Z.; Alves, J.L.F.; da Silva, J.C.G.; Noreen, N.; Iqbal, A. Kinetic and thermodynamics study of the pyrolytic process of the freshwater macroalga, Chara vulgaris. *J. Appl. Phycol.* **2021**, *33*, 2511–2521. [CrossRef]
78. Florentino-Madiedo, L.; Vega, M.F.; Díaz-Faes, E.; Barriocanal, C. Evaluation of synergy during co-pyrolysis of torrefied sawdust, coal and paraffin. A kinetic and thermodynamic study. *Fuel* **2021**, *292*, 120305. [CrossRef]
79. Parthasarathy, P.; Fernandez, A.; Al-Ansari, T.; Mackey, H.R.; Rodriguez, R.; McKay, G. Thermal degradation characteristics and gasification kinetics of camel manure using thermogravimetric analysis. *J. Environ. Manag.* **2021**, *287*, 112345. [CrossRef]
80. Vasudev, V.; Ku, X.; Lin, J. Pyrolysis of algal biomass: Determination of the kinetic triplet and thermodynamic analysis. *Bioresour. Technol.* **2020**, *317*, 124007. [CrossRef] [PubMed]
81. Ni, Z.; Bi, H.; Jiang, C.; Wang, C.; Tian, J.; Zhou, W.; Sun, H.; Lin, Q. Investigation of the co-pyrolysis of coal slime and coffee industry residue based on machine learning methods and TG-FTIR: Synergistic effect, kinetics and thermodynamic. *Fuel* **2021**, *305*, 121527. [CrossRef]
82. Chen, X.; Li, S.; Liu, Z.; Chen, Y.; Yang, H.; Wang, X.; Che, Q.; Chen, W.; Chen, H. Pyrolysis characteristics of lignocellulosic biomass components in the presence of CaO. *Bioresour. Technol.* **2019**, *287*, 121493. [CrossRef]
83. Veses, A.; Sanahuja-Parejo, O.; Navarro, M.V.; López, J.M.; Murillo, R.; Callén, M.S.; García, T. From laboratory scale to pilot plant: Evaluation of the catalytic co-pyrolysis of grape seeds and polystyrene wastes with CaO. *Catal. Today* **2021**, *379*, 87–95. [CrossRef]
84. Lu, Q.; Zhang, Z.-F.; Dong, C.-Q.; Zhu, X.-F. Catalytic Upgrading of Biomass Fast Pyrolysis Vapors with Nano Metal Oxides: An Analytical Py-GC/MS Study. *Energies* **2010**, *3*, 1805–1820. [CrossRef]
85. Wang, D.; Xiao, R.; Zhang, H.; He, G. Comparison of catalytic pyrolysis of biomass with MCM-41 and CaO catalysts by using TGA–FTIR analysis. *J. Anal. Appl. Pyrolysis* **2010**, *89*, 171–177. [CrossRef]
86. Lin, X.; Zhang, Z.; Zhang, Z.; Sun, J.; Wang, Q.; Pittman, C.U. Catalytic fast pyrolysis of a wood-plastic composite with metal oxides as catalysts. *Waste Manag.* **2018**, *79*, 38–47. [CrossRef] [PubMed]

87. Liew, J.X.; Loy, A.C.M.; Chin, B.L.F.; AlNouss, A.; Shahbaz, M.; Al-Ansari, T.; Govindan, R.; Chai, Y.H. Synergistic effects of catalytic co-pyrolysis of corn cob and HDPE waste mixtures using weight average global process model. *Renew. Energy* **2021**, *170*, 948–963. [CrossRef]
88. Park, Y.-K.; Siddiqui, M.Z.; Karagöz, S.; Han, T.U.; Watanabe, A.; Kim, Y.-M. In-situ catalytic co-pyrolysis of kukersite oil shale with black pine wood over acid zeolites. *J. Anal. Appl. Pyrolysis* **2021**, *155*, 105050. [CrossRef]
89. Zhang, X.; Lei, H.; Zhu, L.; Zhu, X.; Qian, M.; Yadavalli, G.; Wu, J.; Chen, S. Thermal behavior and kinetic study for catalytic co-pyrolysis of biomass with plastics. *Bioresour. Technol.* **2016**, *220*, 233–238. [CrossRef]
90. Xu, S.; Cao, B.; Uzoejinwa, B.B.; Odey, E.A.; Wang, S.; Shang, H.; Li, C.; Hu, Y.; Wang, Q.; Nwakaire, J.N. Synergistic effects of catalytic co-pyrolysis of macroalgae with waste plastics. *Process Saf. Environ. Prot.* **2020**, *137*, 34–48. [CrossRef]
91. Dai, M.; Yu, Z.; Fang, S.; Ma, X. Behaviors, product characteristics and kinetics of catalytic co-pyrolysis spirulina and oil shale. *Energy Convers. Manag.* **2019**, *192*, 1–10. [CrossRef]
92. Shahdan, N.A.; Balasundram, V.; Ibrahim, N.; Isha, R.; Manan, Z.A. Catalytic Co-pyrolysis of empty fruit bunch and high-density polyethylene mixtures over rice husk ash: Thermogravimetric, kinetic and thermodynamic analyses. *Clean. Eng. Technol.* **2022**, *9*, 100538. [CrossRef]
93. Rasam, S.; Azizi, K.; Moraveji, M.K.; Akbari, A.; Soria-Verdugo, A. Insights into the co–pyrolysis of olive stone, waste polyvinyl chloride and Spirulina microalgae blends through thermogravimetric analysis. *Algal Res.* **2022**, *62*, 102635. [CrossRef]
94. Wu, Z.; Zhang, J.; Zhang, B.; Guo, W.; Yang, G.; Yang, B. Synergistic effects from co-pyrolysis of lignocellulosic biomass main component with low-rank coal: Online and offline analysis on products distribution and kinetic characteristics. *Appl. Energy* **2020**, *276*, 115461. [CrossRef]
95. Wang, Z.; Burra, K.G.; Lei, T.; Gupta, A.K. Co-pyrolysis of waste plastic and solid biomass for synergistic production of biofuels and chemicals-A review. *Prog. Energy Combust. Sci.* **2021**, *84*, 100899. [CrossRef]
96. Park, D.K.; Kim, S.D.; Lee, S.H.; Lee, J.G. Co-pyrolysis characteristics of sawdust and coal blend in TGA and a fixed bed reactor. *Bioresour. Technol.* **2010**, *101*, 6151–6156. [CrossRef] [PubMed]
97. Tauseef, M.; Ansari, A.A.; Khoja, A.H.; Naqvi, S.R.; Liaquat, R.; Nimmo, W.; Daood, S.S. Thermokinetics synergistic effects on co-pyrolysis of coal and rice husk blends for bioenergy production. *Fuel* **2022**, *318*, 123685. [CrossRef]
98. Ali, I.; Naqvi, S.R.; Bahadar, A. Kinetic analysis of Botryococcus braunii pyrolysis using model-free and model fitting methods. *Fuel* **2018**, *214*, 369–380. [CrossRef]
99. Ashraf, A.; Sattar, H.; Munir, S. A comparative applicability study of model-fitting and model-free kinetic analysis approaches to non-isothermal pyrolysis of coal and agricultural residues. *Fuel* **2019**, *240*, 326–333. [CrossRef]
100. Zhou, L.; Zhang, G.; Zhang, L.; Klinger, D.; Meyer, B. Effects of Contact Conditions between Particles and Volatiles during Co-Pyrolysis of Brown Coal and Wheat Straw in a Thermogravimetric Analyzer and Fixed-Bed Reactor. *Processes* **2019**, *7*, 179. [CrossRef]
101. Nyoni, B.; Duma, S.; Bolo, L.; Shabangu, S.; Hlangothi, S.P. Co-pyrolysis of South African bituminous coal and Scenedesmus microalgae: Kinetics and synergistic effects study. *Int. J. Coal Sci. Technol.* **2020**, *7*, 807–815. [CrossRef]
102. Lu, K.-M.; Lee, W.-J.; Chen, W.-H.; Lin, T.-C. Thermogravimetric analysis and kinetics of co-pyrolysis of raw/torrefied wood and coal blends. *Appl. Energy* **2013**, *105*, 57–65. [CrossRef]
103. Balasundram, V.; Ibrahim, N.; Kasmani, R.M.; Hamid, M.K.A.; Isha, R.; Hasbullah, H.; Ali, R.R. Thermogravimetric catalytic pyrolysis and kinetic studies of coconut copra and rice husk for possible maximum production of pyrolysis oil. *J. Clean. Prod.* **2017**, *167*, 218–228. [CrossRef]
104. Ding, G.; He, B.; Yao, H.; Kuang, Y.; Song, J.; Su, L. Synergistic effect, kinetic and thermodynamics parameters analyses of co-gasification of municipal solid waste and bituminous coal with CO_2. *Waste Manag.* **2021**, *119*, 342–355. [CrossRef]
105. Ali, I.; Tariq, R.; Naqvi, S.R.; Khoja, A.H.; Mehran, M.T.; Naqvi, M.; Gao, N. Kinetic and thermodynamic analyses of dried oily sludge pyrolysis. *J. Energy Inst.* **2021**, *95*, 30–40. [CrossRef]
106. Banyhani, Z.M.; Khan, W.U.H.; El-Gawad, H.H.A.; Anwar, M.; Khoja, A.H.; Hassan, M.; Liaquat, R.; El-Bahy, Z.M. Synergistic transformation: Kinetic and thermodynamic evaluation of co-pyrolysis for low-rank bituminous coal and polyurethane foam waste. *Process Saf. Environ. Prot.* **2024**, *184*, 907–921. [CrossRef]
107. Khoja, A.H.; Gohar, H.; Khan, W.U.H.; Qazi, U.Y.; Din, I.U.; Al-Anazi, A.; Ashraf, W.M.; Mujtaba, M.A.; Riaz, F.; Daood, S.S. Exploring copyrolysis characteristics and thermokinetics of peach stone and bituminous coal blends. *Energy Sci. Eng.* **2023**, *11*, 4302–4323. [CrossRef]